Mobilization of geochemical elements in the active layer of permafrost to surface water in Russian Arctic

Xianchuan Xie[1], Xiaowen Ji[2], Evgeny Abakumov[3], and Vyacheslav Polyakov[4]

[1]Nanjing University
[2]School of Environment and Sustainability, University of Saskatchewan
[3]Saint-Petersburg State University
[4]Arctic and Antarctic Research Institute

November 24, 2022

Abstract

The predicted increasing ground temperatures in the Arctic results in the deepening of the active layer and intensification of geochemical processes, which could affect the geochemical composition of surface waters. Determining the responses of the riparian soil systems to surrounding hydrological flows under changing climate conditions is important for understanding the seasonal changes in hydrological processes. Therefore, in this study, one soil core from the study area polygon rim (close to the Taz River, TA) and two soil cores from the riverain terrace (close to the Syoyakha River, SY and Murtyyakha River, MU) in Russian Western Siberia and their supra-permafrost water, adjacent stream flows and river water were sampled for analysis of geochemical elements. The results showed that most elements above their respective detection limits (Mn, Sr, Fe, Mg, Cr, Co, V, Pb, Al and Ca) started to accumulate in the downwards gleyed layer during September–October in response to the deepest thaw in the active layer. This study focused on the highly mobile elements, i.e., Mn, Ca, Mg, Al and Ti, in the deepest layer; and found the transport of organic matter in the upper layer carried these elements to both surface water ponds/flows and supra-permafrost water, and further, to the rivers. The best linear correlation for both stream flows and river water were Mn, which may be a proxy for predicting the processes occurring within the active layer during the annual summer-autumn thaw. Finally, landscapes with different ice contents may experience changes in the elements transported to surface waters.

Supporting information

Mobilization of geochemical elements in the active layer of permafrost to surface water in Russian Arctic

Xiaowen Ji[a,b,c], Evgeny Abakumov[b], Vyacheslav Polyakov[b,d,e], Xianchuan Xie[a*]

[a] *State Key Laboratory of Pollution Control and Resource Reuse, School of the Environment, Nanjing University, Nanjing, 210093, P. R. China*

[b] *Department of Applied Ecology, Saint Petersburg State University, Saint Petersburg, 199178, Russian Federation*

[c] *School of Environment and Sustainability, University of Saskatchewan, Saskatoon SK, S7N 5B3, Canada*

[d] *Arctic and Antarctic Research Institute, Saint Petersburg, 199397, Russian Federation*

[e] *Department of Soil Science and Agrochemistry, Saint-Petersburg State Agrarian University, Pushkin, Saint Petersburg, 19660, Russian Federation*

* Corresponding author's e-mail: xchxie@nju.edu.com

Text S1. The detailed description of pH values for supra-permafrost water in TA, SY, and MU for different sampling months.

For all periods, the supra-permafrost waters were very acidic with the pH values ranging from 4.06 to 4.93 for Ta, from 3.80 to 4.83 for Sy, and from 3.70 to 4.86 for Mu. In spring the pH values ranged from 4.06 to 4.20 (mean = 4.13) for Ta, from 3.80 to 3.89 (mean = 3.84) for Sy, from 3.70 to 3.96 (mean = 3.81) for Mu. During early June to end of August, the pH ranged from 4.2 to 4.57 (mean = 4.40) for Ta, from 3.81 to 4.57 (mean = 4.26) for Sy, and from 3.90 to 4.67 (mean = 4.33) for Mu. During autumn, the pH values ranged from 4.5 to 4.9 (mean = 4.77) for Ta, from 4.34 to 4.83 (mean = 4.62) for Sy, and from 4.15 to 4.86 (mean = 4.65) for Mu. The lowest concentrations for three sites were approximately at the beginning of May, and the highest concentrations for three sites were observed in October 12, 2016.

Text S2. The detailed description of pH values for the surface water surrounding the soil cores for different sampling months.

Ta exhibited acidity (pH = 6.31-6.85) from spring to the late summer in the streams and kept neutral during autumn seasons, except for two dates in late September. For the Taz river, the pH values ranged from 6.82 to 7.15, with the average value of 6.99 from spring to the beginning of summer and decreased beginning late July. From August, pH values showed an increasing trend until the beginning of October, when the pH values reached their peak (pH = 8.14). In Mu, the pH values of streams fluctuated from 6.11 (the beginning of May) to 6.43 (the end of August) and raised dramatically to between 6.91 and 7.15 from September to the middle of October. The Murtyyakha river showed a relatively higher pH value at the end of May (6.91) and middle of June (6.92), during early summertime and gradually increased from the end of summer to the late autumn with the peak value of 7.84. Sy revealed more acidic pH values (5.71-5.92) in the streams during May and kept stable pH values during June to July, while pH values increased significantly in August and gradually increased until October. The Syoyakha river also showed acidity before late autumn, except for two peaks where the pH values were close to 7 in May and June and the highest pH values were observed in the beginning of October (pH = 7.44).

Text S3. CO_2, CH_4 and DOC in the surrounding hydrological streams.

In SY, the average CO2 concentration increased from May (164 μmol L-1) to October (178 μmol L-1). CH4 average concentrations increased from 32 to 37 μmol L-1 from May to October and that of DOC increased from 164 to 178 mg L-1 from May to October. The same increasing trends were observed in MU and TA. During May to October, the average DOC, CO2 and CH4 concentrations for MU rose from 32 mg L-1, 162 μmol L-1 and 5 μmol L-1 to 38 mg L-1, 178 μmol L-1and 11μmol L-1 respectively, which for TA rose from 39 mg L-1, 202 μmol L-1 and 4 μmol L-1 to 61 mg L-1, 288 μmol L-1and 14 μmol L-1 respectively. The apparent increasing time for MU and SY was in August while for TA was in July.

Table S1. EDX results for soil core collected adjacent to Taz river (TA), Syoyakha river (SY), and Murtyyakha (MU) river in Yamal-Nets Autonomous Region. The values are in mg kg^{-1}.

Element	Site close to Taz river (TA)	Site close to Taz river (TA)	Site close to Taz river (TA)	Site close to Taz river
	0-5 cm Ah@	5-10 cm Ah@	10-20 cm B@1	20-30 cm Bh@
Zn	48.80 ± 3.31	45.09 ± 6.19	46.82 ± 6.73	43.93 ± 5.32
Mn	631 ± 78.61	327 ± 38.96	329 ± 47.51	473 ± 43.17
Fe	19568 ± 2374	18821 ± 1805	20644 ± 1287	18989 ± 2386
As	3.66 ± 0.27	2.82 ± 0.39	3.33 ± 0.20	2.60 ± 0.14
Co	61.2 ± 5.78	54.8 ± 3.71	48.9 ± 2.60	30.5 ± 1.67
Cr	39.37 ± 4.76	41.35 ± 4.93	42.79 ± 4.52	40.54 ± 4.27
V	69.92 ± 4.15	69.21 ± 8.50	73.15 ± 10.55	67.97 ± 4.84
Sr	77.88 ± 6.08	77.17 ± 10.11	85.05 ± 11.48	92.56 ± 9.56
Ca	8263 ± 554	7055 ± 1080	10307 ± 650	10294 ± 700
Na	1154 ± 132	1203 ± 112	1280 ± 137	1262 ± 124

Element	Site close to Taz river (TA)	Site close to Taz river (TA)	Site close to Taz river (TA)	Site close to Taz river
Mg	5922 ± 551	6219 ± 751	7049 ± 604	7097 ± 629
Al	18735 ± 1259	18925 ± 1889	20149 ± 2351	18826 ± 992
Ti	1479 ± 146	1585 ± 91	1656 ± 105	1553 ± 179
Cd	0.19 ± 0.01	0.42 ± 0.03	0.44 ± 0.02	0.31 ± 0.05
Pb	29.06 ± 3.99	26.32 ± 1.92	8.60 ± 0.75	13.87 ±1.50
Mo	0.002 ± 2.5×10^{-4}	0.005 ± 6.6×10^{-4}	0.004 ± 6.4×10^{-4}	0.002 ± 2.0×10^{-4}
Tl	5.23 ± 0.73	5.44 ± 0.51	4.24 ± 0.29	6.57 ± 0.56
Cu	4.08 ± 0.29	2.07 ± 0.81	2.07 ± 0.13	2.38 ± 0.16
Ni	7.57 ± 0.74	6.11 ± 0.87	6.77 ± 0.56	7.27 ± 0.91
Ga	0.08 ± 0.011	0.04 ± 0.003	0.08 ± 0.008	0.06 ± 0.007
Rb	0.07 ± 0.012	0.07 ± 0.010	0.06 ± 0.009	0.07 ± 0.011

Table S1. (continued)

	Site close to Taz river (TA)	Site close to Taz river (TA)	Site close to Taz river (TA)	Site close to Taz river (TA)
	0-5 cm Ah@	5-10 cm Ah@	10-20 cm B@1	20-30 cm Bh@
Zr	0.66 ± 0.06	0.56 ± 0.05	0.72 ± 0.10	1.04 ± 0.15
Nb	0.04 ± 5.4×10^{-3}	0.03 ± 3.5×10^{-3}	0.04 ± 5.2×10^{-3}	0.07 ± 6.1×10^{-3}
Th	0.02 ± 0.003	0.02 ± 0.002	0.02 ± 0.004	0.02 ± 0.004
Br	11.14 ± 1.16	10.23 ± 1.29	11.88 ± 1.61	11.14 ± 0.34
K	1964 ± 116	1819 ± 246	2081 ± 189	1999 ± 191
P	0.15 ± 0.012	0.27 ± 0.028	0.29 ± 0.021	0.12 ± 0.016
Y	3.80 ± 0.26	1.33 ± 0.19	2.18 ± 0.15	3.29 ± 0.39
Sc	4.58 ± 0.59	5.04 ± 0.66	5.37 ± 0.37	5.35 ± 0.53
Ce	0.35 ± 0.04	0.18 ± 0.02	0.19 ± 0.03	0.34 ± 0.04
Pr	0.036 ± 3.0×10^{-3}	0.040 ± 3.4×10^{-3}	0.024 ± 2.1×10^{-3}	0.044 ± 6.2×10^{-3}
Nd	0.039 ± 6.0×10^{-3}	0.040 ± 4.6×10^{-3}	0.052 ± 6.6×10^{-3}	0.017 ± 9.2×10^{-4}
Sm	0.004 ± 4.7×10^{-4}	0.003 ± 3.3×10^{-4}	0.003 ± 3.2×10^{-4}	0.001 ±7.4×10^{-5}
Eu	0.002 ± 2.3×10^{-4}	0.005 ± 5.0×10^{-4}	0.005 ± 7.2×10^{-4}	0.003 ± 4.4×10^{-4}
Tb	0.001 ± 1.4×10^{-4}	0.002 ± 1.2×10^{-4}	0.002 ± 1.1×10^{-4}	0.001 ± 1.3×10^{-4}
Dy	0.001 ± 1.8×10^{-4}	0.009 ± 9.7×10^{-4}	0.008 ± 5.3×10^{-4}	0.007 ± 9.2×10^{-4}
Ho	0.003 ± 4.4×10^{-4}	0.003 ± 4.6×10^{-4}	0.005 ± 4.3×10^{-4}	0.003 ± 1.3×10^{-4}
Er	0.012 ± 1.5×10^{-3}	0.007 ± 8.7×10^{-4}	0.013 ± 1.2×10^{-3}	0.008 ± 7.4×10^{-4}
Tm	5.5×10^{-4} ± 6.3×10^{-5}	8.7×10^{-4} ± 9.0×10^{-5}	9.9×10^{-4} ± 5.8×10^{-5}	7.2×10^{-4} ± 1.0×10^{-4}
Yb	0.004 ± 6.0×10^{-4}	0.005 ± 4.2×10^{-4}	0.003 ± 2.2×10^{-4}	0.004 ± 3.5×10^{-4}
Lu	4.2×10^{-4} ± 3.7×10^{-5}	6.5×10^{-4} ± 7.2×10^{-5}	5.2×10^{-4} ± 2.8×10^{-5}	8.6×10^{-4} ± 1.3×10^{-4}

Table S1. (continued)

Element	Site close to Syoyakha river (SY)	Site close to Syoyakha river (SY)	Site close to Syoyakha river (SY)	Site c
	0-6 cm Ah	6-9 cm B@	9-18 cm Bgw@	18-35
Zn	36.4 ± 3.1	35.7 ± 3.2	38.4 ± 3.4	39.3 ±
Mn	1039 ± 89	231 ± 34	628 ± 38	497 ±
Fe	21075 ± 1637	29790 ± 2307	27316 ± 3476	26847
As	0.74 ± 0.08	3.02 ± 0.19	2.65 ± 0.25	2.34 ±
Co	80.4 ± 9.27	40.1 ± 6.07	49.1 ± 5.41	45.7 ±
Cr	25.1 ± 3.79	64.1 ± 4.58	65.0 ± 3.51	62.9 ±

Element	Site close to Syoyakha river (SY)	Site close to Syoyakha river (SY)	Site close to Syoyakha river (SY)	Site c
V	46 ± 6	109 ± 15	111 ± 8	107 ±
Sr	66.9 ± 5.6	73.2 ± 6.2	77.4 ± 5.1	79.7 ±
Ca	6843 ± 1034	5182 ± 304	6011 ± 916	6471
Na	844 ± 57	912 ± 82	985 ± 97	1097
Mg	3442 ± 222	4715 ± 469	4976 ± 768	5037
Al	10839 ± 649	24845 ± 3774	24748 ± 3679	25017
Ti	779 ± 62	2046 ± 241	1960 ± 301	1968
Cd	0.16 ± 0.01	1.43 ± 0.22	1.42 ± 0.20	0.45 ±
Pb	6.02 ± 0.68	22.17 ± 1.31	23.94 ± 2.02	26.08
Mo	0.002 ± 1.9×10^{-4}	1.0 ± 0.1	1.0 ± 0.1	1.0 ±
Tl	4.12 ± 0.63	5.06 ± 0.38	6.01 ± 0.94	6.37 ±
Cu	2.59 ± 0.27	2.11 ± 0.32	4.85 ± 0.45	3.84 ±
Ni	6.53 ± 0.56	9.48 ± 1.15	8.35 ± 0.74	8.77 ±
Ga	0.078 ± 0.011	0.066 ± 0.006	0.063 ± 0.009	0.063
Rb	0.061 ± 0.005	0.051 ± 0.008	0.054 ± 0.005	0.060
Zr	0.89 ± 0.07	10.51 ± 0.80	10.74 ± 1.64	10.94

Table S1. (continued)

	Site close to Syoyakha river (SY)	Site close to Syoyakha river (SY)	Site close to Syoyakha river (SY)	Site close
	0-6 cm Ah	6-9 cm B@	9-18 cm Bgw@	18-35 cm
Nb	0.042 ± 0.004	0.057 ± 0.003	0.038 ± 0.005	0.064 ± 0.
Th	0.024 ± 0.003	0.024 ± 0.003	0.020 ± 0.003	0.033 ± 0.
Sr	24.60 ± 2.64	21.88 ± 1.40	16.33 ± 1.96	20.45 ± 1.
Br	3.66 ± 0.49	5.37 ± 0.81	4.28 ± 0.59	5.37 ± 0.6
K	1964 ± 107	1819 ± 197	2081 ± 328	1999 ± 24
P	0.11 ± 0.009	0.27 ± 0.036	0.13 ± 0.014	0.27 ± 0.0
Y	3.44 ± 0.29	11.24 ± 1.06	11.40 ± 1.41	11.63 ± 0.
Sc	5.53 ± 0.39	15.04 ± 2.17	15.41 ± 2.16	14.94 ± 2.
Ce	0.65 ± 0.093	0.16 ± 0.008	0.28 ± 0.032	0.59 ± 0.0
Pr	0.03 ± 0.004	0.06 ± 0.006	0.02 ± 0.002	0.03 ± 0.0
Nd	0.05 ± 0.006	0.09 ± 0.007	0.08 ± 0.007	0.06 ± 0.0
Sm	0.003 ± 0.0003	0.003 ± 0.0003	0.002 ± 0.0002	0.003 ± 0.
Eu	0.002 ± 0.0001	0.003 ± 0.0002	0.004 ± 00002	0.005 ± 0.
Tb	0.001 ± 0.0002	0.003 ± 0.0002	0.002 ± 0.0002	0.004 ± 0.
Dy	0.005 ± 0.0006	0.007 ± 0.0004	0.010 ± 0.0005	0.007 ± 0.
Ho	0.002 ± 0.0001	0.003 ± 0.0003	0.003 ± 0.0003	0.003 ± 0.
Er	0.013 ± 0.0018	0.009 ± 0.0013	0.010 ± 0.0015	0.011 ± 0.
Tm	0.0009 ± 8×10^{-5}	0.0007 ± 5×10^{-5}	0.0007 ± 1×10^{-4}	0.0004 ± 3
Yb	0.003 ± 5×10^{-4}	0.004 ± 2×10^{-4}	0.006 ± 3×10^{-4}	0.003 ± 4
Lu	0.0003 ± 3×10^{-5}	0.0005 ± 3×10^{-5}	0.0009 ± 5×10^{-5}	0.0006 ± 9

Table S2. Metal/element concentrations (μ g L^{-1}) in soil porewater extracted from the soil cores collected adjacent to Taz river (TA), Syoyakha river (SY), and Murtyyakha (MU) river in Yamal-Nets Autonomous Region.

Depth (cm)	**SY**	**SY**	**SY**	**SY**	**SY**	**SY**	**SY**	**SY**
	Mn	Fe	K	Ca	Na	Mg	Al	Ti
0-6	94	1686	4	411	7	344	976	62
6-9	23	2979	-	259	-	424	2236	184
9-18	50	1639	-	361	-	249	1732	98
18-35	35	1879	-	647	-	252	1751	138
35-40	31	1389		696	-	255	2511	198
Depth (cm)	**MU**	**MU**	**MU**	**MU**	**MU**	**MU**	**MU**	**MU**
	Mn	Fe	K	Ca	Na	Mg	Al	Ti
0-7	10	983	92	338	26	162	945	46
7-25	47	1273	58	387	-	227	1285	123
20-40	30	1120	-	384	-	304	1831	132
40-60	34	1754	-	463	78	377	1714	85
Depth (cm)	**TA**	**TA**	**TA**	**TA**	**TA**	**TA**	**TA**	**TA**
	Mn	Ca	Mg	Al	Ti			
0-5	107	132	829	318	187			
0-10	36	101	808	359	188			
10-20	33	155	705	221	105			
20-30	85	164	752	239	95			
40-50	79	216	708	238	93			
55-70	76	191	774	201	109			
70-83	45	332	1079	406	182			

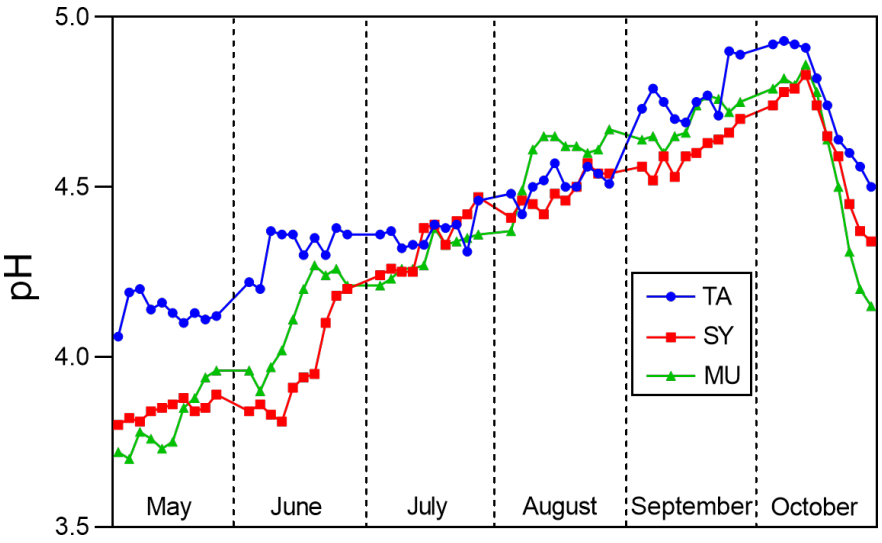

Figure S1. Supra-permafrost water pH values in the Ta, Sy, and Mu sites over course of spring to autumn 2016.

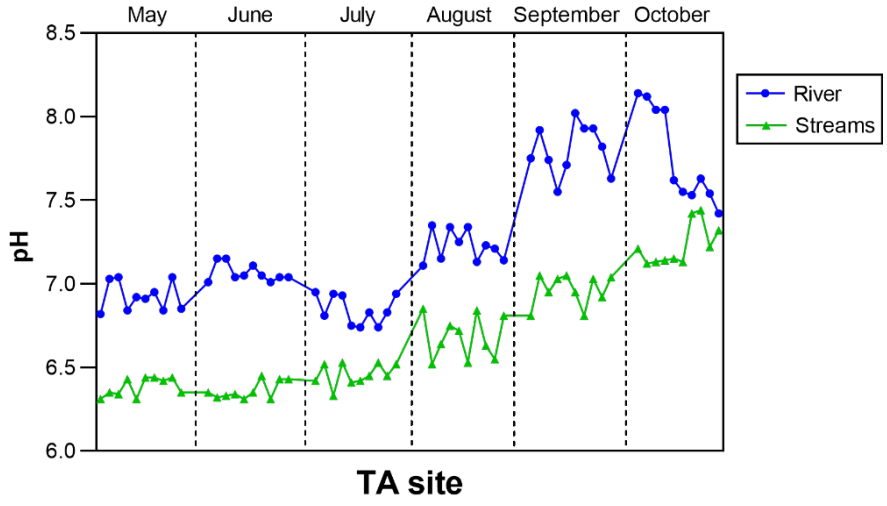

TA site

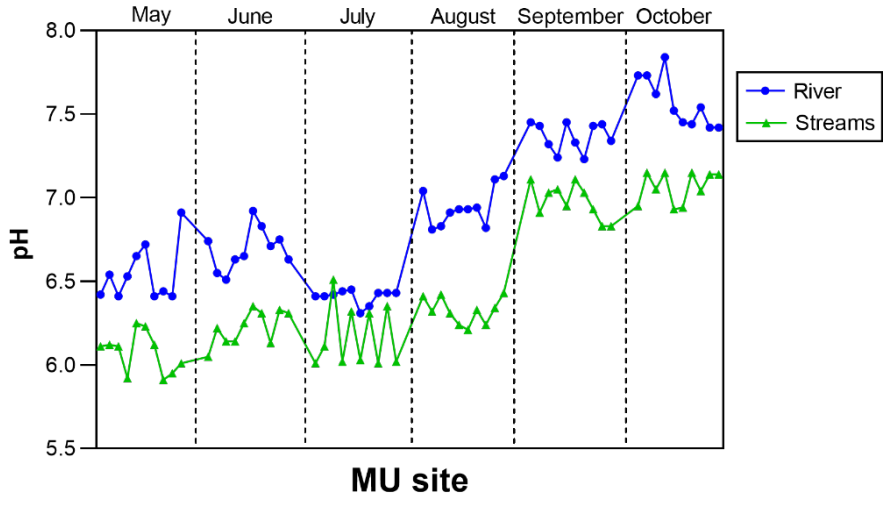

MU site

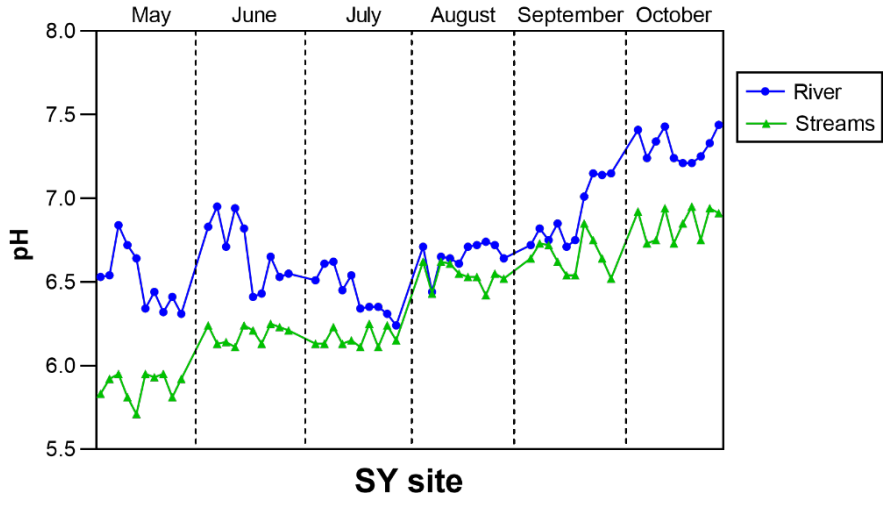

SY site

Figure S2. Surrounding hydrological stream and its received river water pH values in the TA, SY, and MU sites during spring to autumn of 2016.

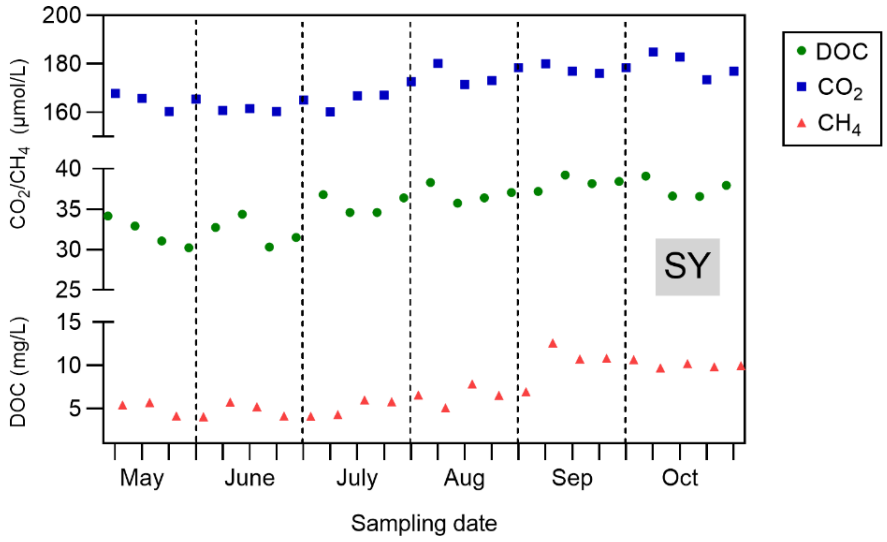

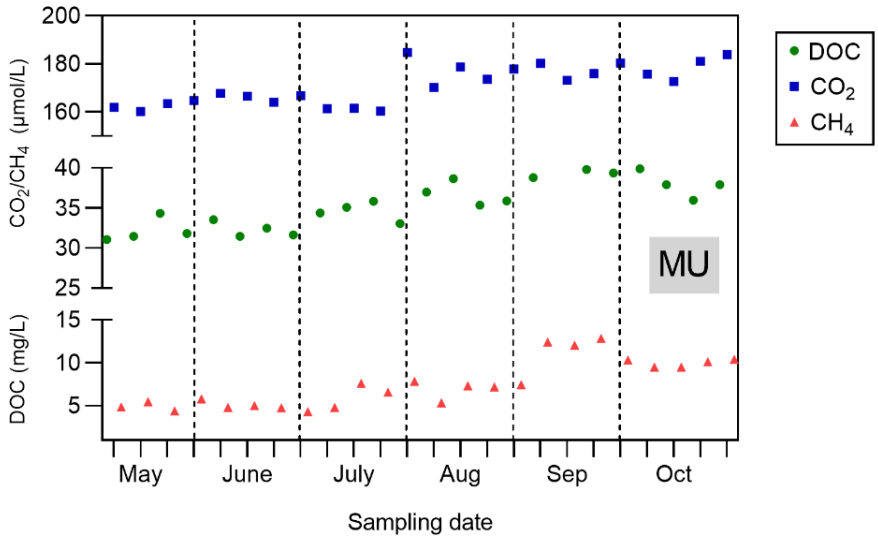

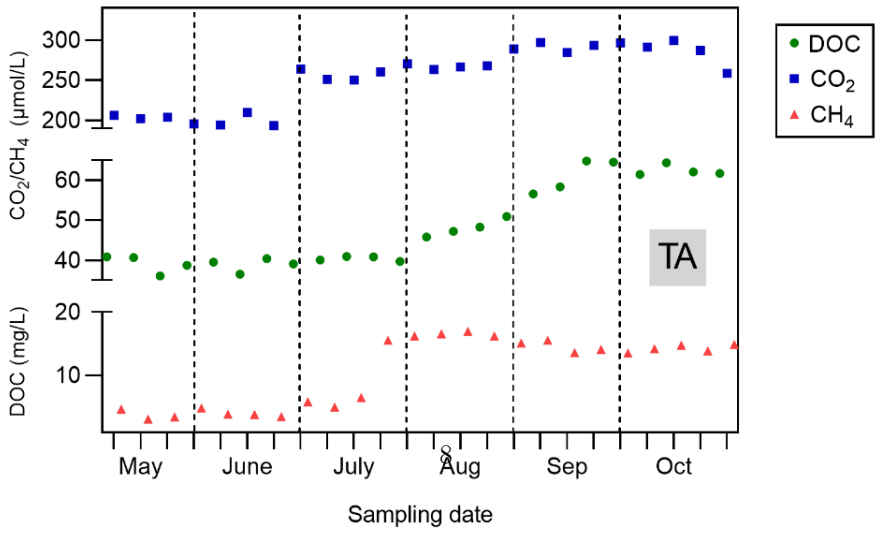

Figure S3. The concentrations of DOC, CO_2 and CH_4 in the surrounding hydrological stream for the TA, SY, and MU sites.

Mobilization of geochemical elements in the active layer of permafrost to surface water in Russian Arctic

Xiaowen Ji[a,b,c], Evgeny Abakumov[b], Vyacheslav Polyakov[b,d,e], Xianchuan Xie[a*]

[a] *State Key Laboratory of Pollution Control and Resource Reuse, School of the Environment, Nanjing University, Nanjing, 210093, P. R. China*

[b] *Department of Applied Ecology, Saint Petersburg State University, Saint Petersburg, 199178, Russian Federation*

[c] *School of Environment and Sustainability, University of Saskatchewan, Saskatoon SK, S7N 5B3, Canada*

[d] *Arctic and Antarctic Research Institute, Saint Petersburg, 199397, Russian Federation*

[e] *Department of Soil Science and Agrochemistry, Saint-Petersburg State Agrarian University, Pushkin, Saint Petersburg, 19660, Russian Federation*

* Corresponding author's e-mail: xchxie@nju.edu.com

Abstract

The predicted increasing ground temperatures in the Arctic results in the deepening of the active layer and intensification of geochemical processes, which could affect the geochemical composition of surface waters. Determining the responses of the riparian soil systems to surrounding hydrological flows under changing climate conditions is important for understanding the seasonal changes in hydrological processes. Therefore, in this study, one soil core from the study area polygon rim (close to the Taz River, TA) and two soil cores from the riverain terrace (close to the Syoyakha River, SY and Murtyyakha River, MU) in Russian Western Siberia and their supra-permafrost water, adjacent stream flows and river water were sampled for analysis of geochemical elements. The results showed that most elements above their respective detection limits (Mn, Sr, Fe, Mg, Cr, Co, V, Pb, Al and Ca) started to accumulate in the downwards gleyed layer during September–October in response to the deepest thaw in the active layer. This study focused on the highly mobile elements, i.e., Mn, Ca, Mg, Al and Ti, in the deepest layer; and found that the transport of organic matter in the upper layer carried these elements to both surface water ponds/flows and supra-permafrost water, and further, to the rivers. The best linear correlation for both stream flows and river water were Mn, which may be a proxy for predicting the processes occurring within the active layer during the annual summer-autumn thaw. Finally, landscapes with different ice contents may experience changes in the elements transported to surface waters.

Keywords: Geochemical elements, Arctic, Permafrost-affected soils, active layer, surface water, seasonal thawing

Plain Language Summary

The rapid increasing atmospheric temperature in the Arctic has led the feedback of permafrost thawing, which increases the depth of active layer and accelerate chemical weathering. These processes may cause chemical substances further releasing to adjacent aquatic landscapes. Here we investigated the horizontal and vertical transport of geochemical elements through surface flow and supra-permafrost water to river water from three cryogenic soil cores in the Arctic tundra. The results showed that most elements would accumulate in the gleyed layer that was the deepest in the active layer during thawing season. Mn, Ca, Mg, Al and Ti showed the highest mobility from soil to supra-permafrost water to the surface flows/rivers, while Mn was the only element could transport from topsoil and supra-permafrost water to surface water and river, which may be a proxy predicting the processes of active layer during summer-autumn thawing.

1. Introduction

The increasing atmospheric temperatures in the Arctic have led to permafrost thawing and vertical downward migration of the active layer into formerly frozen ground, during the thawing season [*H H Christiansen et al.*, 2010; *R Connon et al.*, 2018; *M T Jorgenson et al.*, 2010; *V E Romanovsky et al.*, 2010; *S L Smith et al.*, 2010]. The active layer responds to the changing climatic conditions by increasing its depth, thus accelerating chemical weathering [*N Colombo et al.*, 2019; *K Keller et al.*, 2007; 2010] and potentially releasing geochemical components and organic carbon from the soil to adjacent aquatic landscapes [*A J Barker et al.*, 2014; *G Grosse et al.*, 2016; *K D Johnson et al.*, 2013; *C E Johnston et al.*, 2014; *S V Loiko et al.*, 2017; *T V Raudina et al.*, 2018; *E A G Schuur et al.*, 2015]. This would increase the movement of carbon dioxide (CO_2) from the soil to aquatic reservoirs such as rivers and lakes [*C D Elder et al.*, 2019; *S M Natali et al.*, 2015; *Y M Polishchuk et al.*, 2018; *B Wild et al.*, 2019]; this occurs through the transport of solute and water along surface streams and the permafrost table, which is as known as "supra-permafrost flow". Supra-permafrost water is found in the shallow subsurface of the active layer, where it is typically situated at the boundary between the frozen and thawed fractions of the soil profile [*D J Cederstrom et al.*, 1953]. Owing to the absence of groundwater discharge in the permafrost-affected region, solutes being transported to lakes or rivers from adjacent soils originate primarily from supra-permafrost water.

Permafrost degradation has been associated with an increased contribution of groundwater to stream via surface flows or supra-permafrost water in Canadian Arctic rivers [*M A Walvoord and R G Striegl*, 2007]. Ice wedge degradation has also been proven to be related to the water balance of lowland across the Arctic landscapes, and to increase streamflow [*A K Liljedahl et al.*, 2016]. Several studies have observed substantial increments in discharges from the major Eurasian Arctic rivers due to the warming climate [*N J Browny et al.*, 2019; *D Feng et al.*, 2019; *R B Lammers et al.*, 2001; *D Q Yang et al.*, 2002; *L Zheng et al.*, 2019]. *T V Raudina et al.* [2018] observed a northward shift of the permafrost boundary under climate change scenarios, and that the concentrations of dissolved organic carbon (DOC), major and trace elements, and greenhouse gases are expected to decrease in the supra-permafrost waters at the border between the thawed

and frozen parts from peat soils in the western Siberia lowland. *S V Loiko et al.* [2017] hypothesized that the direct mobilization of soil waters to hydrological networks and the transformation of autochthonous processes were controlled by physical factors in different landscapes. Overall, there appears to be considerable variability and uncertainty regarding how discharges of DOC, elements, and greenhouse gases in supra-permafrost waters/surface flows respond to permafrost thaw and are released to surface water ponds and rivers.

Several studies concerning the biogeochemical cycles of carbon and related metals focused on both the aquatic and the terrestrial parts of the continental permafrost-bearing ecosystem [*L Guo et al.*, 2007; *J W McClelland et al.*, 2007; *D Olefeldt and N T Roulet*, 2012; *O S Pokrovsky et al.*, 2011]. More recently, the biogeochemistry of soil porewater and supra-permafrost water in mineral and organic/peat parts of soil profiles in the permafrost areas have been studied [*A J Barker et al.*, 2014; *S Jessen et al.*, 2014; *D Lamhonwah et al.*, 2017; *S V Loiko et al.*, 2017; *T V Raudina et al.*, 2018; *L E Street et al.*, 2016]. The previous studies concluded that the export fluxes of DOC, greenhouse gases, and trace metals from the active layer of permafrost to the surrounding hydrological landscapes are determined by the amount of water passing through the active layer till the border of the frozen permafrost, before being drained to a lake or river [*Oleg S. Pokrovsky et al.*, 2016; *O. S. Pokrovsky et al.*, 2016; *T V Raudina et al.*, 2018]. *A J Barker et al.* [2014] reported that the concentrations of metals in surface water were related to the increasing active layer thickness/degrading permafrost during late fall and early winter. These results revealed that the dynamics of trace metal concentrations in the transitions from Arctic soils to surface water corresponded to top-down freezing processes in the active layer. However, there is a lack of information connecting geochemical tracers in both the underlying supra-permafrost flow and the upper soil layer to explain the transport of geochemical compositions to surrounding hydrological networks and can be used as a proxy for the seasonal active layer dynamics.

Therefore, this study aims to provide this knowledge by analyzing supra-permafrost water, soil pore water, surrounding small water ponds/flows, and eventually, river surface water from three typical soils close to rivers from continuous permafrost regions within the Yamal and Gydan peninsulas, West Siberian Arctic. Tundra lakes and river floodplains are abundant in the Yamal and Gydan peninsulas; lakes cover, on average, 10% of the Yamal peninsula, occupying 20% of the

floodplains of large rivers [*Y A Dvornikov et al.*, 2019]. Approximately 90% of all lakes in the study region are small (<1 km^2) water bodies. To analyze the effluxes of permafrost soils from relatively homogeneous landscapes, the sampling sites were set up next to the largest rivers flowing to the Kara sea, such as the Syoyakha, Murtyyakha, and Taz Rivers. Our main working hypotheses are as follows: (*i*) Based on the response of riverine DOC and element concentrations to increasing active layer thickness reachs the highest contents during late autumn, when the active layer reaches its greatest depth in a year. Besides, when the components' concentrations in the base flow increases, with the yearly maximum values being observed in the Siberian rivers [*D Q Yang et al.*, 2002]. Therefore, the dominant contributor of DOC and trace elements to river waters during this time of the year is expected to be supra-permafrost water and base flow to the rivers. (*ii*) When mineral weathering processes continue in the deeper soil column during late autumn and early winter, shallow subsurface soil can also store major mobilized components, such as DOC, in late autumn during freezing; these components bind with elements and can contribute to spring thaw in the next year. Formerly mobilized components stored in the shallow subsurface during spring snowmelt can be potentially enhanced to supra-permafrost waters and further to surrounding surface waters. Therefore, with an increasing thawed depth of permafrost and the potentially enhanced mineral weathering fluxes into supra-permafrost waters, biogeochemical fluxes from surrounding surface waters may experience a change during spring and autumn. (*iii*) As the DOC and elements are controlled by the redox environment of riparian soils, they cannot be consumed by the surrounding biota or depleted by abiotic reaction, and thence persist in supra-permafrost water; they may be transported to the surrounding hydrological network.

The specific objectives of this study were (*1*) to assess the mobility of releasing geochemical elements from upper soil layer water and supra-permafrost water to surrounding water bodies; (*2*) to examine whether the concentrations of geochemical elements in the surface water (connected streams and received river) can explain the active layer dynamics of permafrost riparian soils in different permafrost-affected landscapes.

2. Studying site and methods

2.1 Geographical setting

The study area was located in the Northwest area of the Yamal-Nets Autonomous Region, across 66° N, with continuous permafrost (**Figure 1A**). Sampling sites were located close to the lowlands of the Syoyakha, Murtyyakha, and Taz rivers. The Syoyakha and Murtyyakha Rivers are situated in the Yamal Peninsula on the Western Siberian plain [*M Golovatin et al.*, 2011]. These geographical features of this region are strongly divided between river valleys, lake hollows, and streams [*M Golovatin et al.*, 2011]. Cryogenic soils in this part of the Yamal Peninsula were formed due to the high ice content of Holocene alluvial sediments [*A Sidorchuk and V Grigorev*, 1998] and aeolian materials [*I Alekseev and E Abakumov*, 2018]. This part of the lowland comprises very flat watersheds of the Syoyakha and Murtyyakha Rivers and is covered with frozen bogs and palsa. The Syoyakha is one of the largest rivers of the Yamal Peninsula [*Y Bespalaya et al.*, 2018]; its watercourse is 165 km long and its watershed covers an area of 4,400 km^2 [*Y Bespalaya et al.*, 2018]. The Murtyyakha River has roughly 580 watercourses and numerous lakes in its basin, which contains 70 rivers more than 10 km long. The Murtyyakha River flows into the Syoyakha River and then enters Kara Sea. Syngenetic permafrost close to these two rivers contains massive Holocene ice deposits [*Y Vasil'chuk et al.*, 2016]. The 1,401 km long Taz River is located in the Gydan Peninsula and drains a basin of 150,000 km^2; it flows into the Taz Estuary and ends in the Gulf of Ob. Soils along with the river included alluvial stratified parent deposits from an earlier stage of the Holocene [*C Tarnocai*, 2009].

We investigated the three poorly drained riparian soils with upper organic layers and a downward mineral profile adjacent to each river (**Figure 1A**). The soil close to the Taz River site (TA) was located at the top of the polygon rim, where the landscape is polygonal tundra, and the center of polygon was wet-depressed and an accumulation of organic matter poorly degraded by anaerobic conditions; the surrounding elevated polygon rim showed the evidence

of cryoturbation in most horizons in the active layer (**Figure 1B**). The soil profile was gleyed with frost heaving of the clay stratum. The surrounding vegetation consists predominantly of wet acidic tussock sedge, grass, and sphagnum moss. Soils sampled nearby at the Syoyakha (SY) and Murtyyakha (MU) Rivers were both situated from the floodplain. The SY site consisted of moist acidic moss, lichen, and sedges, and MU site consisted of lingonberry, willow, moss, and sedge. Both soil profiles had shallow active layers that were strongly gleyed and under reducing conditions, while the deeper layers at MU showed obvious signs of cryoturbation (**Figure 1C and D**). The formation of the SY and MU stratified soils may have resulted from the constant changes in the river water levels. All three soil profiles for TA, SY, and MU have been depicted as relatively light chroma color with oxidation of iron minerals and dominated by mineral substrates with allochthonous organic matter or autochthonous peat.

2.2 Soil core and supra-permafrost water collection and analysis

Three soil cores were extracted up to the permafrost table using a portable Snow-Ice Permafrost-Research-Establishment (SIPRE) auger set consisting of a coring auger and an engine from Jon's Machine Shop, Fairbanks, Alaska, USA. The location of each soil core was directly adjacent to the borehole into which a string thermometer was inserted (**Figure 1A**). The thermometers, which were put in cases filled with grease as an inert material, were placed roughly 10 cm from permafrost table for 24 h in July 2016 in order to reach thermal equilibrium with surrounding soil material. The thermometers were connected to a data logger for recording hourly temperatures in degrees Celsius (Modular GM10, Yokogawa Electric Corporation, Tokyo, Japan), powered by a battery with a three-year life and attached to a stainless-steel stake inserted into the soil cores. The excavated local soils were moved back to the soil cores. The cores were collected in May 2016, sealed with Polyethylene covers, transported at a stable temperature of -4 ℃ to freeze the soils, and stored in a refrigerator at the same temperature prior to analysis. We believe the cores can partially reflect the deepest active layer during a year, with approximately 65 cm for Mu, 46 cm for Sy, and 90 cm for Ta

189 shown by the thawing materials. The soil pits were excavated in July 2017 adjacent to the
190 coring location (**Figure 1**), and site restoration procedures followed the standard protocols for
191 permafrost-affected soils [*C-L Ping et al.*, 2013]. Excavating soil pits may provide an insight
192 into the vertical depth between the active layer and permafrost that contain external flows to
193 rivers. Each 35 × 35 cm soil pit was excavated with a shovel and hatchet until reaching frozen
194 materials and the genetic horizon and name of each soil were identified using the World
195 Reference Base for Soil Resources *WRB* [2015] classification system. The stagnic condition
196 of soils meant that we had to use 2,2'-Dipyridyl to spray soils for 30 s to test for reducing
197 conditions, as per the tests previously conducted on gleyed soils [*C L Ping et al.*, 1998].
198 The frozen soil core was cut into 5 cm sections with a diamond wire saw (LKH-8, Kanghua
199 Company, Guilin, China), with a cutting section of diamond-impregnated wire mounted on
200 idler pulleys, in a cold room in the laboratory of Arctic Logistics Center, Salekhard,
201 Yamal-Nenets Autonomous Region, Russia. The cut sections of each soil core were then
202 placed in tightly sealed plastic bags (9.5 cm x 18 cm, Bag Whirlpak Clear 7oz, Nasco, FL, US)
203 and kept at room temperature (approximately 23 ℃) to thaw for 12 h. Completely thawed
204 soils were used to collect soil porewater with an SPS 200 lysimeter soil solution sampler
205 (SDEC, Reignac-sur-Indre, France). The collected water was filtered through a 0.45 μm
206 polypropylene filter, decanted to glass test tubes, and acidified with 0.5(wt) % ultrapure nitric
207 acid (HNO_3, CAS: 7697-37-2 Fisher Scientific, Hampton, USA) before processing through
208 inductively coupled plasma-tandem mass spectrometry (8800 ICP-MS/MS, Agilent, Santa
209 Clara CA, USA). To remove the spectral interferences of ions through icon/neutral reactions,
210 the collision reaction cells (CRCs) mode in the ICP-MS was operated using He or NH_3 as the
211 inert collision gas, following the protocol developed by *E McCurdy and G Woods* [2004]. The
212 elements V, Cr, Mn, Fe, Co, Ni, Cu, Zn, and As were analyzed in CRCs mode with He gas to
213 remove unidentified polyatomic particles arising from the variables Cl^-, S^-, and C^-. Ti was
214 analyzed in CRCs mode with NH_3 to remove interference from S-based polyatomic ions. The
215 elements Sr, K, Ca, Mg, Al, Ba, Be, B, Cd, Pb, Au, Mo, P, Sc, Ag, Tl, Sn, and rare earth

elements (REEs) were analyzed using normal (non-CRCs) mode.

Four calibration standards (1×10^{-2}, 1×10^{-1}, 1×10^{1}, 1×10^{2} μg L^{-1}) were prepared by diluting 1×10^{3} μg L^{-1} stock standard solution for each element and mixed REEs (TraceCERT®) purchased from Sigma-Aldrich, St. Louis MO USA. The 2% (w/w) ultrapure HNO_3 was taken as the blank. Calibration was performed before every analytical test with a good calibration curve ($R^2 \approx 0.999$), and three blanks and check standards were run before every ten samples. The analytical uncertainty for each sample was determined by the analysis of triplicate within an error of ± 3%. The detection limits for all elements were set at the level of 1 μg L^{-1}. To correct the magnitude of the signal suppression or enhancement, a standard mixture solution of Bi, Ge, In, Li, Sc, Tb, and Y (10 μg /mL) prepared in 2% ultrapure HNO_3 was used as the internal standard added in all standards, blanks, and samples.

Then, each soil core section was transported to the Applied Ecological Laboratory, Saint Petersburg State University. They were dried in a vacuum drying oven for 16 h, homogenized by grinding using a roller mill, processed through a 2-mm sieve, and finally, soils were pressed into a powder pellet with a vertical hydraulic jack. Each pellet was analyzed through scanning electron microscopy with energy dispersive X-ray spectroscopy (SEM-EDX) (JSM-6390 LA, EX2300, JEOL, Tokyo, Japan). EDX revealed the characteristic peak for each metal in each sample with atomic-level precision, which can directly transfer the concentration in terms of mg kg^{-1}. The soil certified reference material CRM027 and SQC001-30G (Sigma-Aldrich, St. Louis, USA) for trace metals were used for calibration. Samples and the reference material were analyzed in triplicate, and the detection limits were determined based on the minimum value of the reference material.

The location of stagnant supra-permafrost waters was collected adjacent to the previous soil cores in September 2016. To prevent the contamination of water samples due to the previous methods of collecting supra-permafrost waters with soil pit excavation, an alloy probe rod was first inserted into the soil to confirm approximately the same depth of the active layer–permafrost boundary as the previous soil core. A direct push device (SP16

243 Groundwater Sampler, Geoprobe Systems®, Salina KS USA) comprising a polyvinyl
244 chloride screen was driven to the permafrost table within a sealed steel sheath. Then, the
245 water samples were pumped through the tube to the surface and stored in 25-mL PVC serum
246 bottles by oscillating the tubing up and down.

247 For the lower floodplain (SY and MU), water samples were collected after pumping the
248 tube for 15–20 min to flush water with permafrost materials. The time required for pumping
249 water in TA was relatively longer than that for the other sites, by approximately 30 min, with
250 less volume of inflowing water because of the higher depth of polygon rim. For all sites, the
251 first portion of water containing permafrost materials was discarded, and the clearer water
252 with fewer impurities was collected. Unfiltered water Samples in the serum bottles were
253 treated with 0.2 mL of mercuric chloride ($HgCl_2$, Sigma-Aldrich) and capped without air
254 bubbles or headspace using butyl rubber stoppers pierced by a needle attached to a 3-mL
255 syringe that allows air and water escape from the bottle when the stopper is inserted. With the
256 bottle inverted, 10 ml of methane-free helium (Sigma-AldricFh) was added, meanwhile 10 ml
257 of water was removed through needle displacement and the syringe. Then, another 10 ml of
258 methane-free helium was added to the headspace without removing water, and water and
259 headspace were equilibrated in the bottle by shaking for 2 min. The triplicates of subsample
260 headspace gas (into the syringe) were analyzed for CH_4 and CO_2 by gas chromatography
261 (GC-456, Bruker, Billerica MA, USA), with flame-ionization detection (FID) and electron
262 capture detection (ECD), respectively. After each set of ten samples, the detectors were
263 calibrated based on Air Liquide (CO_2 = 246.6 μmole/mole, CH_4 = 302.3 μmole/mole). The
264 results of triplicate injection showed a repetition rate within ±2%. The gas solubility of CH_4
265 and CO_2 [*P Kastanidis et al.*, 2018] were taken by calculating the total concentration of CH_4
266 and CO_2 in the vials and then converting to μmol/L of the initial samples. All analysis
267 procedures for analyzing CH_4 and CO_2 were carried out in the Center for Chemical Analysis
268 and Materials Research of St. Petersburg State University. The water temperature, dissolved
269 oxygen, pH, and specific conductivity were field measured with a portable multiparameter

meter (Orion Star™ A329, ThermoFischer Scientific, Waltham MA, USA). Stagnant supra-permafrost waters in this study were oxygenated with an average O_2 saturation in samples ranging from 10.2 to 82.3% with an uncertainty of 3-4%, which is very close to the previous reports in Western Siberian lowlands [*S V Loiko et al.*, 2017; *T V Raudina et al.*, 2018]. No significant difference was observed in the O_2 concentrations from water samples in each soil site. The average temperature of supra-permafrost waters did not vary significantly as 12.3±1.8 ℃ for SY, 13.4±1.6 ℃ for MU, and 15.6±2.0 ℃ for TA. The dissolved organic carbon (DOC) concentrations were analyzed by a TOC-L TOC Analyzer (Shimadzu Kyoto, Japan) with an uncertainty of 5% and a detection limit of 4 μg/L.

2.3 Surface water collection and analysis

All surface water samples were collected in September 2016. All sampling sites were adjacent to the location of the soil cores. We collected water samples (streams connected to each river) from shallow (< 10-30 cm) permafrost subsidence and hollows with the size of < 1 m^2; deep depressions (< 1 m) of palsa bogs with sizes ranging from 5 to 15 m^2; small thaw ponds with sizes ranging 10-150 m^2; and each river closest to the soil core within 5–10 m (depth < 5 m). Neoprene gloves were used during water sampling, and water from the shoreside was collected by a standard PVC MP^2 two-stop peristaltic pump tubing (1.09 mm I.D., White/Red, Pkg. 12, PerkinElmer, Waltham MA, USA) outfitted with a pre-sterilized Durapore® 0.45 μm capsule filter (MilliporeSigma, Burlington MA, USA). The water passing through the tubing and filter capsules for the first 30 s was not collected, and polypropylene (PPCO) bottles with white PP closure precleaned by 2% nitric acid were used for water collection. The analysis of trace metals in water samples was the same as in subchapter 2.2. The samples used for chloride determination were not acidified. Chloride determination was performed by titration with silver nitrate ($AgNO_3$, 0.02 mol L^{-1}) as titrant according to ISO 9297: 2000 “Water quality — Determination of chloride — Silver nitrate titration with chromate indicator (Mohr's method).” Titrant calibration was used by

296 standardizing $AgNO_3$ solution versus NaCl solution with the same molar concentration (0.02
297 mol L^{-1}). The relative standard deviation (RSD) of titrant was <1 %.

298 # 3. Results

299 ## 3.1 Characteristics of soil profile and chemical composition in the soil column

300 The detailed horizon and vegetation information in the soil pit profiles in the photographs
301 for SY, MU, and TA is shown in **Figure 1**. The soil group belongs to Histic Gleysols
302 (Stagnic), Histic Gleysols (Turbic), and Turbic Cryosols for SY, MU, and TA, respectively.
303 The top fractions of soil horizons from three soil pits all show a high chroma color, with TA
304 being relatively lighter (**Figure 1B**), and all the lower fractions show strong gleyed conditions,
305 which may indicate a redox boundary. The lower fractions of soils were further tested by a
306 few drops of alpha-alpha-dipyridyl for 30–40 s, showing that no pink color was observed for
307 SY at the depth of 6–9 cm, with a strip-shaped iron oxidized boundary to the next horizon. A
308 positive pink color was observed during the reaction in the next gray color horizon (9-18 cm),
309 suggesting the occurrence of reduced ferrous oxides under the reducing condition. Compared
310 with the previous horizon, this horizon had few plant roots and little accumulation of organic
311 matter. The lowest section (18-35 cm depth) had a sporadic positive pink color. This
312 difference may be due to the different redox spots visually observed in the excavated soil pit
313 (**Figure 1C**). The lower 18–35 cm showed heterogeneous rusty-gray color as the ferric irons,
314 as well as aluminum, and inclusions of organic materials due to the cryogenic mass exchange
315 through bottom-up transportation of water by thawing/freezing processes that bring parent
316 materials to the upper layers, where cracks can be observed in 18–35 cm. In the upper 6–9 cm
317 horizon, the oxidation of ferrous iron to ferric iron is mostly due to the leaching process of
318 upper thawing water containing oxygen. Therefore, the low density of strictly reduced gleyed
319 horizon (6-9 cm) separated the two different geochemical transport pathways between the
320 upper and lower horizons.

321 For soil pit MU, the pink reaction color was observed at the depth of 7–25 cm (the shape

shown as $B_{g@}$ horizon in **Figure 1D**), and the middle part of depth 25–60 cm and 60–65 cm depth. In the $B_{g@}$ horizon, there were more disbursed rust-orange spots and stains that followed the path of roots; these ferrous irons were oxidized by the atmosphere through the growth upper vegetation's roots growing. In the 25–60 cm depth, the apparent presence of cryoturbation with a gray-brown color was observed alongside the dark-gray inclusions from the lower permafrost. The oxidized iron in this horizon results from the multi-year freezing/thawing and lower activities of congeliturbation that transport the materials from both the upper and lower layers. The 60–65 cm depth was completely under the reducing condition with loamy soils in gray color.

For soil pit TA, the reducing conditions indicated by a positive pink color were observed below 55 cm. TA shows a mixed O and A horizon within 30 cm that has a brownish-gray color and very few roots, which is common under hummocks in Western Siberia. Within the 0–55 cm depth, the lateral ring-shaped layers and mud spots can be observed, which were caused by frost heave when a rounded knoll of ice rises during the freezing time. The evidence of cryoturbation can be seen below 55 cm with the dark gray color, and some moss residues are observed in the fragments of cryoturbation clusters.

The vertical elemental concentrations in three soil cores measured by EDX are listed in **Table S1** (**Supporting Information**) and plotted as logarithmic concentrations in soil core depth in **Figure 2**. The other elements not shown in **Figure 2** did not exhibit a regular pattern under reducing conditions within the soil cores. Mn and Co were enriched in the top mineral layer with organic matter accumulation, which likely because of their complexation with natural organic matter. In contrast, Cr, V, Sr, Ca, Mg, Al, Ti, Cd, Mo, Zr, and Sc increased in lower mineral soil horizons in the three soil cores. In particular, for the MU site, Fe, Cr, and V were only higher in the first gleyed horizon with cryoturbation (7-25 cm) and decreased gradually with increased depth. Al, Ti, Cd, and Sc kept increasing until 40 cm (second gleyed horizon) and then decreased gradually or maintained relatively comparable levels in the deeper layers. As, Mo, and Zr decreased until 40 cm and then increased in deeper mineral

horizons mixed with frozen material and at the frozen horizon. Zn, Sr, K, Ca, Na, Mg, and Y were higher in all gleyed horizons.

For the SY site, three trends were observed: *i*) relatively slight decrease from top to down within the gleyed horizons for As, Cr, V, Mo, Zr, and Se; *ii*) continuous increase in gleyed horizon depth for Sr, K, Ca, Va, Mg, Al, Ti, and Pb; *iii*) only the Cd content increased sharply in the upper gleyed horizon (9–18 cm) and decreased significantly below 18 cm. For the TA site, the maximum concentration was observed in the gleyed horizon for Cr, V, Sr, Ca, Mg, Al, Ti, Cd, Pb, Mo, Zr, Y, and Sc. These elements were apparently enhanced in reducing fractions, concentrations of which, with respect to the upper layers of soil column, can reflect the soils with increased reducing soil conditions. This obvious demarcation between elements with concentrations either increasing in the upper layers of soil column or accumulating in the lower part of soil column correlates to the variation of redox conditions in the soil pit profile as well. The fluctuation of elemental concentrations in the lower soil cores may also be caused by the effect of cryoturbation.

The elemental concentrations of soil porewater are listed in **Table S2** and plotted as the function of depth along the cores (not containing supra-permafrost water) in **Figure 3**. The results showed Ca, Mg, and Ti as soluble species that may be available for transporting supra-permafrost water for all three sites because of the increased concentrations in the deeper fraction of the soil core. Additionally, Al in TA site, Mg in MU site, and Fe in SY site may also have the same potential. To some extent, Mn, Ca, Mg, Al, Ti, and Fe all can be soluble species in both upper and deeper fractions of the soil core, indicating both the transport capability from surface flows and supra-permafrost waters to the river.

3.2 Thermal dynamics within soil depth

The temperatures in multiple depths from the installed thermometers are provided in **Figure 4**. In general, the surface (0 cm) soil temperature corresponds to the variation in ambient temperature in this region. The soils at four different depths in TA, MU, and SY were completely frozen by the end of April as our measurements were initiated. In TA, the thawing

of frozen soils (temperature rose above 0 ℃) occurred on May 30, 2016 at 0 cm, on June 7, 2016 at 20 cm, on June 18, 2016 at 40 cm, and on June 30, 2016 at 75 cm. In MU, the thawing occurred on June 2, 2016 at 0 cm, on July 14, 2017 at 25 cm, on June 25, 2016 at 40 cm, and on July 4, 2016 on 59 cm. In Sy, the thawing occurred on June 1, 2016 at 0 cm, on June 11, 2016 at 18 cm, on June 22, 2017 at 26 cm, and on July 2, 2016 at 38 cm. The frozen soils in the Arctic notably thaw from top down during the spring-summer season. The lower latitude of TA results in a relatively earlier thawing time than that of MU and SY.

3.3 Chemical composition in the supra-permafrost water

All measured elemental concentrations are plotted as the function of sampling time in **Figure 5 and** the pH values for supra-permafrost water in TA, SY, and MU for different sampling months are presented in **Figure S1** with a detailed description in **Text S1**. In TA, the contents of Zn, Mn, Ti, and Sr increased generally from the beginning of summer (June) while Sr and Ti increased slightly with an obvious increasing trend at the end of summer (September 15, 2016). Zn reached its highest concentrations (15.93-17.50 μg L^{-1}) at the beginning of autumn, and this level was maintained until October 2016. Unlike Zn, the peak value of Mn was observed in October. Fe concentrations started to rise significantly at the end of September and peaked at the end of October 2016 (2049.71 μg L^{-1}). Mg, Cr, V, Pb, Al, and Ca concentrations exhibited less fluctuation over summer with low concentrations until an increasing trend was observed at the beginning of autumn. Na was the only element that showed a gradual increase in concentration over time till October 15, 2016. For Cd and Mo, there was no particular trend, and their levels were low. SY and MU essentially followed the pattern of TA, while the highest Fe concentration in SY was found at the end of October 2016.

3.4 Chemical composition in the surrounding hydrological streams and rivers

We measured the elemental concentrations of the surface water surrounding the soil cores, including the connected hydrological flows (i.e., shallow, depression, and thaw ponds) and

rivers (the sites receive the flow), which are shown in **Figure 6**. The pH values for TA, MU, and SY for different months are shown in **Figure S2** with detailed description in **Text S2**. The concentrations of CO_2, CH_4, and DOC in the surrounding streams are plotted as the function of sampling time in **Figure S3** and described in **Text S3**.

The remaining detected elements were not shown here because they were below the detection limits. The three sites showed strong similarity of elements' distribution in the connected surface flows and the adjacent rivers with the passage of time. Most elements (i.e., Fe, Mn, Zn, Na, Pb, Al, and Ca) showed a dramatically increasing trend from the beginning of September to the beginning of October, while Co, V, and Sr significantly increased beginning in August, and only Cr increased starting in July. These elements in the surrounding hydrological streams or rivers reached their highest concentrations at the beginning of October, except for Mo, Cd, and Ti, which had very low concentrations at all time-scales with a slightly increased concentration in October. The concentrations of Fe, Zn, Al, Co, and Sr were consistent with the observation of enhanced soluble concentrations in supra-permafrost water for each of the corresponding months. This may be because of the solubility of these metals, except Co and Mn, which remained at low levels in the top layers of soil cores, and because of the different solubilities of the metals during snow melting, which are related to the bonding mechanism in the soil, especially for top soil layers with increased organic matter. The highest to lowest concentrations for metals were approximately Fe > Mn > Zn > Sr > Ti > V ≈ Na ≈ Al ≈ Pb > Cd ≈ Mo.

4. Discussion

4.1 Variability of elemental concentrations in solid soil and soil porewater

In the TA soil column, higher elemental concentrations in soil porewater, such as Mn, Mg, and Ti, were found in the oxidizing zone (~10-15 cm, the layer with organic matter accumulations). Compared with the deeper depth of soil column (~30-83 cm, reducing zone),

enhanced elemental accumulations were also observed, especially for Mg and Ti. The lesser extent of Ca and Al concentrations in the top organic layer (**Figure 2**), which may be due to the excess of Ca in the soil solutions, occupy more than 90% of total cation concentration [*J O Leckie*, 1986]. Ca cation can control the soluble stage of trace elements in soils, due to Ca's presentation as an organic complex in soil solutions, preventing the precipitation of soil deposits [*J O Leckie*, 1986]. For instance, fulvic acid in this organic layer can significantly interfere with the crystallization of aluminum hydroxide polymorphs [*H Kodama and M Schnitzer*, 1980]. Besides, the aqueous Ti concentrations in both the oxidizing and reducing zones are similar, while Mn is relatively higher in oxidizing zones, and Mg is more enhanced in the reducing zone. Compared with the distribution of these elements in the solid soil core, only Ca and Al showed a similar trend. This difference is due to the soluble and chemical fraction of species.

In MU soil column, the concentrations of Mn, Ca, Mg, Al, Fe, and Ti in soil porewater were increased below 7 cm in the reduced zones. However, the solid soil phase shows high levels of Mn in the oxidizing zones (~0-7 cm), with the other elements' distribution corresponding to the soluble forms. In SY soil column, Mn, Mg, and Fe contents in soil porewater were enhanced in the upper oxidizing zones, and Ca content was only obviously enhanced in reduced zones, while Al and Ti both accumulated in the oxidizing and reduced zones. The Mn concentrations were found to be the highest in the oxidizing zones in solid phase, whereas other elements (Ca, Mg, Al, Ti, and Fe) increased in the reduced zones.

In both MU and SY, Mn concentrations are found higher in top layer of soil, which is consistent with the low solubility of Mn in lower pH soils (pH = 4.7 for Mu and 4.8 for Sy) [*F Scholz and H Kahlert*, 2015]. We speculate this is because of a more integral gleyed layer (~ 10-40 cm) caused by cryoturbation, which makes the soils share the same origin. SY revealed more heterogenous materials that divided several soil layers through cryoturbation, which results in elemental fluctuations in terms of soluble elements.

The three soil cores' depth represents the typical maximum vertical extent during the

thawing period in autumn. Among the three soil cores, differences between elemental concentrations in soil porewater and solid soil are still substantial. Taking as an example the concentrations of Mn in the Ta soil column, the concentration of Mn in the oxidizing layer is 1039 mg/kg^{-1} with approximately 0.11 mg/L^{-1} in soluble form. There is approximately 0.045 mg/L^{-1} mobilized within thawing water to the reduced zones with 388 mg kg^{-1} presented in solid soil of this layer.

To better understand the solubility of elements, the partitioning coefficients (K_d) were calculated as shown in **Figure 7**. Despite the discrepancy of K_d below the top layer, the decreasing solubility can be observed within the gleyed layers, which is consistent with the theory that metals are hindered in this layer [*I Antcibor et al.*, 2014]. However, Al and Mn were observed with clearly increasing solubility in all soil cores above the permafrost table. Besides, the high partitioning from the solid to the aqueous fraction was observed in Ti for Sy, and Fe and Mn for Mu. Unlike the top organic-rich layers mainly reflecting biogeochemical cycle, minerogenic layers reflect mineralogical weathering. Therefore, the difference may be due to different soil textures and frost processes.

The enrichment of Mn and Al for soil materials in Western Siberia was previously investigated [*E Abakumov et al.*, 2017; *I Antcibor et al.*, 2014; *L Evgeny et al.*, 2017; *X Ji et al.*, 2019a; *X Ji et al.*, 2019b]. The further soil water flows into supra-permafrost water, the more it creates consistent input of elements such as Mn and Al from soil to solution. The previous study showed that the solubility of Mn increases with increasing soil acidity [*E Andrade et al.*, 2002], which is consistent with our observation. *A J Barker et al.* [2014] first reported that trace metals concentrations (Al, Ba, Fe, and Mn) correlate with the seasonal thawed active layer in the Alaskan arctic. This also proves that elemental transport occurred through thawing soil porewater with the potential for those elements to enter surrounding water bodies.

4.2 Elemental fluctuation in supra-permafrost water and surface water by seasonal controls

To some extent, except for Mn and Al, some other elements also showed high solubility in the bottom of the three soil cores (**Figure 7**). We expected to see high mobilization of Mn, Al, Ca, and Ti to the supra-permafrost water during spring snow thawing. However, except for Mn, no or very slightly increasing concentrations in the late May / beginning of June can be found in the supra-permafrost water (**Figure 5**), which may be due to the low volume of thawing water or the equilibrium between elemental pool size in solid soils and snowmelt water in the reducing zones at this time. We found the peak concentration time for most elements were shown in late autumn / the beginning of winter. Compared with elements in soil porewater, more elements were above the detection limits and at distinguishable higher levels during the August to October time period. This may indicate that the origin of elements in supra-permafrost water may not only originate from the dilution of snowmelt water within the soil core, while other water flows through the slope of the permafrost table in the landscape. The relatively higher levels of elements such as Mn, Zn, and Fe in TA, than that of SY and MU, could result from the frost heaving of the polygon rim, which released more frozen materials. During summer, thawing starts in the permafrost-affected soils leading to a deeper active layer, which can be shown by the slight increase in Mn, Fe and other elemental concentrations in the supra-permafrost water over the course of June, July, and August. This increase is correlated with the low coefficients in the bottom of the soil core, and with the soil temperature as well. The soil thermal stratification shows that soil temperatures were above 0 °C at 0, 20, and 40 cm for TA from late June; in 0, 25, and 40 cm for MU from beginning June; and in 0, 18, and 25 cm for SY from late June whereas the deeper depth (75 cm for TA, 59 for MU, and 38 for SY) was still frozen at this time.

Most elements revealed relatively high solubility with small K_d values at the deepest depth. In Ta, Mn follows this trend at the depth 18-35 cm, whereas at the deeper depth of 35-40 cm the solubility decreases. The high mobility of these elements in the deeper soil column, along

with the latter thawing for these layers, could account for high concentrations in supra-permafrost water and surface water in late September and beginning of October. This pattern is relatively comparable to other elements in TA, MU, and SY, except for Ca and Ti in MU. Generally, elemental fluctuations in the surface flow and river were the same as the supra-permafrost water. The concentrations of Zn, Mn, and Ti in the rivers from July to October were higher than the surface flow, indicating the mobility of these elements to the rivers from the surface flow and include the possibility of contribution to this input from supra-permafrost water. The previous study also showed some metals like Fe, Al, Mn, and Ba decreased in the active layer with subsequent thawing and increasing surface water concentrations during summer to autumn and could indicate elemental transport signals corresponding to the depth dynamics of the active layer [*A J Barker et al.*, 2014]. Our results are consistent with the theory that major and trace elements export to the lakes and rivers through the boundary between the thawed and frozen layers [*T V Raudina et al.*, 2018]. However, we cannot exclude the possibility of abrupt permafrost collapse in the surrounding water body and rivers, which has been shown to enhance metals release into surface water [*S V Loiko et al.*, 2017]. This may also be a reason that not all elements in the surface water were above the detection limits in the soil porewater.

4.3 Potential elemental signatures as a function of organic matter in the surface flow

The discharge and source of water are important for the transport of geochemical components such as elements and organic carbon to surface waters. However, it is difficult to determine water sources in cryogenic landscapes with large amounts of ice and multiple flows. In the present study, DOC is used as the “participating media” to estimate elements transported to the surface water; these are considered to be the major carriers of trace elements in boreal and permafrost-affected organic-rich surface waters [*B Lyvén et al.*, 2003; *Q Ma et al.*, 2019; *E Neubauer et al.*, 2013; *R D Rember and J H Trefry*, 2004; *E V*

532 *Vasyukova et al.*, 2010]. Due to no pollution from domestic and industrial activities in our
533 sampling sites, the riverine organic carbon is usually subdivided into two origins as the
534 allochthonous pool derived from terrestrial organic matter (topographical erosion and soil
535 leaching) and the autochthonous pool derived from in-situ phytoplankton production [*D Hope*
536 *et al.*, 1994]. Additionally, an empirical model for organic carbon exports showed DOC
537 exports to surface runoff is mostly driven by the unfrozen zones during permafrost thawing
538 [*C Fabre et al.*, 2019]. Therefore, the surface streams with smaller water volume connected
539 between the soils and the rivers were investigated for the relationships between DOC and
540 elements, and the elemental relationship among the streams, rivers, and supra-permafrost
541 waters.

542 The soil in the three study fields all have a top organic layer with sporadic organic
543 distributions in the mineral layers. Previous studies reported that precipitations would form in
544 the rapid surface runoff through supper soil layers with a depth of approximately 15–20 cm
545 [*K H Bishop et al.*, 1993; *D Hope et al.*, 1994]. DOC would be exported to the surface water
546 from the top layer without infiltration in the riparian zone. In TA, the highest concentrations
547 of CO_2 and CH_4 were observed in the summer snowmelt season with an increasing thawing
548 degree while low concentrations were observed (**Figure 8**), which may have been due to an
549 abrupt thawing process from the top organic layer. This was consistent with the maximal
550 microbial metabolism occurring at the boundary between thawed and frozen permafrost soils
551 in the Western Siberia lowland [*Y N Morgalev et al.*, 2017]. However, *P J Dillon and L A*
552 *Molot* [1997] reported that the release of CO_2 into the boreal waters was increased when the
553 DOC concentration was elevated in the thermokarst lakes. We found a slight decrease in CO_2
554 and CH_4 when the DOC concentrations reached its peak in Autumn in TA. However, a
555 different pattern was observed in SY and MU in that CO_2 and CH_4 did not increase
556 significantly during snow-ice melting in the spring and summer seasons, while an increasing
557 trend was observed for DOC contents in the surface water. *R M Manasypov et al.* [2015]
558 reported no significant enrichment of CO_2 and CH_4 in the thermokarst water bodies during the

559 spring flood through the base flow and further observed that CO_2 levels only increased in
560 small depressions (<10 m^2), which is consistent with the ponds (approximately 1 m^2) that we
561 sampled. Although some obvious buildup of CO_2 was found in the summer for SY, the results
562 are still comparable to the phenomena in high latitude lakes [*J Karlsson et al.*, 2013]. The
563 reason for the contrast between TA and the other sites (SY and MU) could be caused by the
564 low volume of the water pond in SY, and in MU due to the low ice contents and a short
565 period suitable for this type of accumulation in low elevations. However, there is also a
566 possibility that more ice existing in polygon rim and buried talik would lead more the more
567 unfrozen water flowing to the surrounding streams. Combination of the results of three sites
568 shows that the response mechanism of enhancing CO_2 in the streams during snow melting is
569 heterotrophic respiration of allochthonous DOM, as approved by the constantly elevated DOC
570 concentrations in this period. However, we suggest the bio-utilization of these carbon types in
571 small ponds may vary according to the contents of materials by different water volumes.
572 The elements with high mobility in the bottom gleyed layer of the soil column and obvious
573 higher concentrations during the snowmelt period were plotted against the DOC (**Figure 8**).
574 In Ta, Mn increased sharply in the summer while Al, Ca, and Mg did not significantly
575 increase. Peak values of Mn, Al, Ca, and Mg with DOC were observed in autumn. The same
576 pattern was observed for SY and MU, especially for Mn. This may indicate the release of
577 micronutrients as Mn during vegetation activity and upper moss litter leaching in the warmer
578 water, which allows higher mobility within the soil column. Because we did not observe a
579 high concentration of Mn in the uppermost soil layer (**Figure 2**), we speculate this
580 contribution of Mn may be from the supra-permafrost water.
581 Another difference found in the TA site was that elemental concentrations (Al, Ca, and Mg)
582 in autumn were significantly higher in comparison to MU and SY, which may be a result of
583 upwelling via the icy cracks beginning as early as October, producing organic- and
584 Fe-accumulated allochthonous ice crystallized at the pond surface. The maximum values of
585 these elements peak during autumn in the surface water are about 2 to 3 times greater than in

spring and summer, representing the highest water flow including DOC and dissolved elements.

Additionally, the strong linear correlation of Mn between surface streams and rivers was found for all three sites, and that of Al between the surface streams and river was found for Ta (**Figure 9**). However, when comparing the surface streams and supra-permafrost water, Mn was correlated for all three sites; Al only for TA and SY; and Ca only for TA (**Figure 10**). For Mn, the snowmelt flows had higher Mn contents attributed to the increasing mobility of Mn species to other elements in superficial layers of soil as previously reported [*A J Barker et al.*, 2014]. Supra-permafrost water also initially contributes to the surface flows and then further flows to the river. The differences for Al and Ca may be due to the different water–soil interactions. Therefore, Mn could be a seasonal signature of autumn representing the dominance of overland surface flow and maximum interactions with the active layer when the active layer is the deepest.

5. Conclusion

This study found that the levels of elements did not begin to increase when the surface temperature is above 0 ℃, and the deeper soil column temperature is above 0 ℃ in late summer/early autumn. The patterns for surrounding water ponds, adjacent river surface waters, and supra-permafrost waters were generally comparable for most elements above detection limits (Zn, Mn, Sr, Fe, Mg, Cr, Co, V, Pb, Al, and Ca) and were highest during the period from September to October, corresponding to the deepest depth of the active layer. Although a geochemical barrier in the reducing gleyed layers was observed in the soil column, some elements (Mn, Ca, Mg, Al, and Ti) still have high mobility above the permafrost table. Additionally, Mn may flow into surrounding water flows (to the river) by both upper soil and supra-permafrost waters transporting organic matter including CH_4 and CO_2. However, heterogenous landscapes with more ice and cryoturbation may cause more elements to move to the surface waters in the present study. Mn in surface flow may be a proxy for the active

layer process during the period of summer and autumn. Highly dynamic Arctic hydrological systems that receive geochemical elements from surrounding permafrost soils and delivering more DOC and elements to adjacent hydrological systems. Future climate conditions will intensify the soil–stream–river process due to permafrost degradation and the dynamics of the active layer.

Acknowledgements

This work was supported by a grant from the Russian Foundation for Basic research (18-44-890003, 16-34-60010 and 19-416-890002); by Jiangsu Nature Science Fund (BK20151378) and the Fundamental Research Funds for the Central Universities (090514380001); by a grant from Saint-Petersburg State University "Urbanized ecosystems of the Russian Arctic: dynamics; state and sustainable development (grant number: 39377455)". We would like to thank Miss Yu Su from the School of Visual Arts at BFA Computer Art for helping with data visualization, and Miss Kuznetsova Ekaterina from School of Journalism and Communication, Tsinghua University for helping with the Russian translation. Datasets for this research are available through Ji, Xiaowen (2020), “Data of Chemical analysis from soil cores and surface waters from Yamal-Nets Area”, Mendeley Data, v1 http://dx.doi.org/10.17632/hhhns8sptr.1.

References

Abakumov, E., G. Shamilishviliy, and A. Yurtaev (2017), Soil polychemical contamination on Beliy Island as key background and reference plot for Yamal region, in *Polish Polar Research*, edited, p. 313.

Alekseev, I., and E. Abakumov (2018), Permafrost-affected former agricultural soils of the Salekhard city (Central part of Yamal region).

Andrade, E., M. Miyazawa, M. A. Pavan, and E. L. d. Oliveira (2002), Effect of Organic Matter on Manganese Solubility, *Brazilian Archives of Biology and Technology*, *45*, 17-20.

Antcibor, I., A. Eschenbach, S. Zubrzycki, L. Kutzbach, D. Bolshiyanov, and E. M. Pfeiffer (2014), Trace metal distribution in pristine permafrost-affected soils of the Lena River delta and its hinterland, northern Siberia, Russia, *Biogeosciences*, *11*(1), 1-15.

Barker, A. J., T. A. Douglas, A. D. Jacobson, J. W. McClelland, A. G. Ilgen, M. S. Khosh, G. O. Lehn, and T. P. Trainor (2014), Late season mobilization of trace metals in two small Alaskan arctic watersheds as a proxy for landscape scale permafrost active layer dynamics, *Chemical Geology*, *381*, 180-193.

Bespalaya, Y., O. Aksenova, and N. Zubriy (2018), Molluscan fauna of the lower reaches of the Syoyakha River (Yamal Peninsula), *Arctic Environmental Research*, *18*, 76-81.

Bishop, K. H., U. S. Lundström, and R. Giesler (1993), Transfer of organic C from forest soils to surface waters: example from northern Sweden, *Appl. Geochem.*, *8*, 11-15.

Browny, N. J., J. Nilsson, and P. Pemberton (2019), Arctic Ocean Freshwater Dynamics: Transient Response to Increasing River Runoff and Precipitation, *Journal of Geophysical Research-Oceans*, *124*(7), 5205-5219.

Cederstrom, D. J., P. M. Johnston, and S. Subitzky (1953), Occurrence and development of ground water in permafrost regions, *Report Rep. 275*.

Christiansen, H. H., et al. (2010), The thermal state of permafrost in the nordic area during the international polar year 2007–2009, *Permafrost and Periglacial Processes*, *21*(2), 156-181.

Colombo, N., et al. (2019), Influence of permafrost, rock and ice glaciers on chemistry of high-elevation ponds (NW Italian Alps), *Sci. Total Environ.*, *685*, 886-901.

Connon, R., E. Devoie, M. Hayashi, T. Veness, and W. Quinton (2018), The Influence of Shallow Taliks on Permafrost Thaw and Active Layer Dynamics in Subarctic Canada, *Journal of Geophysical Research-Earth Surface*, *123*(2), 281-297.

Dillon, P. J., and L. A. Molot (1997), Dissolved organic and inorganic carbon mass balances in central Ontario lakes, *Biogeochemistry*, *36*(1), 29-42.

Dvornikov, Y. A., et al. (2019), Gas-emission craters of the Yamal and Gydan peninsulas: A proposed mechanism for lake genesis and development of permafrost landscapes, *Permafrost and Periglacial Processes*, *30*(3), 146-162.

Elder, C. D., M. Schweiger, B. Lam, E. D. Crook, X. Xu, J. Walker, K. M. W. Anthony, and C. I. Czimczik (2019), Seasonal Sources of Whole-Lake CH4 and CO2 Emissions From Interior Alaskan Thermokarst Lakes, *Journal of Geophysical Research-Biogeosciences*, *124*(5), 1209-1229.

Evgeny, L., V. Beznosikov, and E. Abakumov (2017), Humic substances elemental composition of selected taiga and tundra soils from Russian European North-East, *Polish*

671 *Polar Research*, *38*, 125-147.
672 Fabre, C., S. Sauvage, N. Tananaev, G. E. Noël, R. Teisserenc, J. L. Probst, and J. M. S. Pérez
673 (2019), Assessment of sediment and organic carbon exports into the Arctic ocean: The case of
674 the Yenisei River basin, *Water Res.*, *158*, 118-135.
675 Feng, D., C. J. Gleason, X. Yang, and T. M. Pavelsky (2019), Comparing Discharge Estimates
676 Made via the BAM Algorithm in High-Order Arctic Rivers Derived Solely From Optical
677 CubeSat, Landsat, and Sentinel-2 Data, *Water Resour. Res.*
678 Golovatin, M., L. M. Morozova, S. N. Ektova, and S. P. Paskhalny (2011), The change of
679 tundra biota at yamal peninsula (the north of the Western Siberia, Russia) in connection with
680 anthropogenic and climatic shifts, *Tundras: Vegetation, Wildlife and Climate Trends*, 1-46.
681 Grosse, G., S. Goetz, A. D. McGuire, V. E. Romanovsky, and E. A. G. Schuur (2016),
682 Changing permafrost in a warming world and feedbacks to the Earth system, *Environmental*
683 *Research Letters*, *11*(4), 040201.
684 Guo, L., C.-L. Ping, and R. W. Macdonald (2007), Mobilization pathways of organic carbon
685 from permafrost to arctic rivers in a changing climate, *Geophysical Research Letters*, *34*(13).
686 Hope, D., M. F. Billett, and M. S. Cresser (1994), A review of the export of carbon in river
687 water: Fluxes and processes, *Environ. Pollut.*, *84*(3), 301-324.
688 Jessen, S., H. D. Holmslykke, K. Rasmussen, N. Richardt, and P. E. Holm (2014), Hydrology
689 and pore water chemistry in a permafrost wetland, Ilulissat, Greenland, *Water Resour. Res.*,
690 *50*(6), 4760-4774.
691 Ji, X., E. Abakumov, and V. Polyakov (2019a), Assessments of pollution status and human
692 health risk of heavy metals in permafrost-affected soils and lichens: A case-study in Yamal
693 Peninsula, Russia Arctic AU - Ji, Xiaowen, *Human and Ecological Risk Assessment: An*
694 *International Journal*, 1-18.
695 Ji, X., E. Abakumov, I. Antcibor, V. Tomashunas, C. Knoblauch, S. Zubzycki, and E.-M.
696 Pfeiffer (2019b), Influence of Anthropogenic Activities on Metals in Arctic Permafrost: A
697 Characterization of Benchmark Soils on the Yamal and Gydan Peninsulas in Russia, *Archives*
698 *of Environmental Contamination and Toxicology*, *76*(4), 540-553.
699 Johnson, K. D., J. W. Harden, A. David McGuire, M. Clark, F. Yuan, and A. O. Finley (2013),
700 Permafrost and organic layer interactions over a climate gradient in a discontinuous
701 permafrost zone, *Environmental Research Letters*, *8*(3), 035028.
702 Johnston, C. E., S. A. Ewing, J. W. Harden, R. K. Varner, K. P. Wickland, J. C. Koch, C. C.
703 Fuller, K. Manies, and M. T. Jorgenson (2014), Effect of permafrost thaw on CO2and
704 CH4exchange in a western Alaska peatland chronosequence, *Environmental Research Letters*,
705 *9*(8), 085004.
706 Jorgenson, M. T., V. Romanovsky, J. Harden, Y. Shur, J. O'Donnell, E. A. G. Schuur, M.
707 Kanevskiy, and S. Marchenko (2010), Resilience and vulnerability of permafrost to climate
708 change, *Canadian Journal of Forest Research*, *40*(7), 1219-1236.
709 Karlsson, J., R. Giesler, J. Persson, and E. Lundin (2013), High emission of carbon dioxide
710 and methane during ice thaw in high latitude lakes, *Geophysical Research Letters*, *40*(6),
711 1123-1127.
712 Kastanidis, P., V. K. Michalis, G. E. Romanos, A. K. Stubos, I. G. Economou, and I. N.
713 Tsimpanogiannis (2018), Solubility of Methane and Carbon Dioxide in the Aqueous Phase of
714 the Ternary (Methane + Carbon Dioxide + Water) Mixture: Experimental Measurements and

715 Molecular Dynamics Simulations, *Journal of Chemical & Engineering Data*, *63*(4),
716 1027-1035.
717 Keller, K., J. D. Blum, and G. W. Kling (2007), Geochemistry of Soils and Streams on
718 Surfaces of Varying Ages in Arctic Alaska, *Arctic, Antarctic, and Alpine Research*, *39*(1),
719 84-98.
720 Keller, K., J. D. Blum, and G. W. Kling (2010), Stream geochemistry as an indicator of
721 increasing permafrost thaw depth in an arctic watershed, *Chem. Geol.*, *273*(1), 76-81.
722 Kodama, H., and M. Schnitzer (1980), Effect of fulvic acid on the crystallization of aluminum
723 hydroxides, *Geoderma*, *24*(3), 195-205.
724 Lamhonwah, D., M. J. Lafrenière, S. F. Lamoureux, and B. B. Wolfe (2017), Evaluating the
725 hydrological and hydrochemical responses of a High Arctic catchment during an
726 exceptionally warm summer, *Hydrological Processes*, *31*(12), 2296-2313.
727 Lammers, R. B., A. I. Shiklomanov, C. J. Vorosmarty, B. M. Fekete, and B. J. Peterson (2001),
728 Assessment of contemporary Arctic river runoff based on observational discharge records,
729 *Journal of Geophysical Research-Atmospheres*, *106*(D4), 3321-3334.
730 Leckie, J. O. (1986), Adsorption and Transformation of Trace Element Species at
731 Sediment/Water Interfaces, paper presented at The Importance of Chemical "Speciation" in
732 Environmental Processes, Springer Berlin Heidelberg, Berlin, Heidelberg, 1986//.
733 Liljedahl, A. K., et al. (2016), Pan-Arctic ice-wedge degradation in warming permafrost and
734 its influence on tundra hydrology, *Nature Geoscience*, *9*(4), 312-+.
735 Loiko, S. V., O. S. Pokrovsky, T. V. Raudina, A. Lim, L. G. Kolesnichenko, L. S. Shirokova, S.
736 N. Vorobyev, and S. N. Kirpotin (2017), Abrupt permafrost collapse enhances organic carbon,
737 CO2, nutrient and metal release into surface waters, *Chem. Geol.*, *471*, 153-165.
738 Lyvén, B., M. Hassellöv, D. R. Turner, C. Haraldsson, and K. Andersson (2003), Competition
739 between iron- and carbon-based colloidal carriers for trace metals in a freshwater assessed
740 using flow field-flow fractionation coupled to ICPMS, *Geochim. Cosmochim. Acta*, *67*(20),
741 3791-3802.
742 Ma, Q., H. Jin, C. Yu, and V. F. Bense (2019), Dissolved organic carbon in permafrost regions:
743 A review, *Science China Earth Sciences*, *62*(2), 349-364.
744 Manasypov, R. M., et al. (2015), Seasonal dynamics of organic carbon and metals in
745 thermokarst lakes from the discontinuous permafrost zone of western Siberia, *Biogeosciences*,
746 *12*(10), 3009-3028.
747 McClelland, J. W., M. Stieglitz, F. Pan, R. M. Holmes, and B. J. Peterson (2007), Recent
748 changes in nitrate and dissolved organic carbon export from the upper Kuparuk River, North
749 Slope, Alaska, *Journal of Geophysical Research: Biogeosciences*, *112*(G4).
750 McCurdy, E., and G. Woods (2004), The application of collision/reaction cell inductively
751 coupled plasma mass spectrometry to multi-element analysis in variable sample matrices,
752 using He as a non-reactive cell gas, *J. Anal. At. Spectrom.*, *19*(5), 607-615.
753 Morgalev, Y. N., et al. (2017), Bacteria primarily metabolize at the active layer/permafrost
754 border in the peat core from a permafrost region in western Siberia, *Polar Biology*, *40*(8),
755 1645-1659.
756 Natali, S. M., et al. (2015), Permafrost thaw and soil moisture driving CO 2 and CH 4 release
757 from upland tundra, *Journal of Geophysical Research: Biogeosciences*, *120*(3), 525-537.
758 Neubauer, E., S. J. Köhler, F. von der Kammer, H. Laudon, and T. Hofmann (2013), Effect of

pH and Stream Order on Iron and Arsenic Speciation in Boreal Catchments, *Environmental Science & Technology*, *47*(13), 7120-7128.
Olefeldt, D., and N. T. Roulet (2012), Effects of permafrost and hydrology on the composition and transport of dissolved organic carbon in a subarctic peatland complex, *Journal of Geophysical Research: Biogeosciences*, *117*(G1).
Ping, C.-L., M. H. Clark, J. M. Kimble, G. J. Michaelson, Y. Shur, and C. A. Stiles (2013), Sampling Protocols for Permafrost-Affected Soils, *Soil Horizons*, *54*(1).
Ping, C. L., J. G. Bockheim, J. M. Kimble, G. J. Michaelson, and D. A. Walker (1998), Characteristics of cryogenic soils along a latitudinal transect in Arctic Alaska, *Journal of Geophysical Research-Atmospheres*, *103*(D22), 28917-28928.
Pokrovsky, O. S., R. M. Manasypov, S. V. Loiko, and L. S. Shirokova (2016), Organic and organo-mineral colloids in discontinuous permafrost zone, *Geochim. Cosmochim. Acta*, *188*, 1-20.
Pokrovsky, O. S., L. S. Shirokova, S. N. Kirpotin, S. Audry, J. Viers, and B. Dupre (2011), Effect of permafrost thawing on organic carbon and trace element colloidal speciation in the thermokarst lakes of western Siberia, *Biogeosciences*, *8*(3), 565-583.
Pokrovsky, O. S., R. M. Manasypov, S. V. Loiko, I. A. Krickov, S. G. Kopysov, L. G. Kolesnichenko, S. N. Vorobyev, and S. N. Kirpotin (2016), Trace element transport in western Siberian rivers across a permafrost gradient, *Biogeosciences*, *13*(6), 1877-1900.
Polishchuk, Y. M., A. N. Bogdanov, I. N. Muratov, V. Y. Polishchuk, A. Lim, R. M. Manasypov, L. S. Shirokova, and O. S. Pokrovsky (2018), Minor contribution of small thaw ponds to the pools of carbon and methane in the inland waters of the permafrost-affected part of the Western Siberian Lowland, *Environmental Research Letters*, *13*(4).
Raudina, T. V., S. V. Loiko, A. Lim, R. M. Manasypov, L. S. Shirokova, G. I. Istigechev, D. M. Kuzmina, S. P. Kulizhsky, S. N. Vorobyev, and O. S. Pokrovsky (2018), Permafrost thaw and climate warming may decrease the CO2, carbon, and metal concentration in peat soil waters of the Western Siberia Lowland, *Sci. Total Environ.*, *634*, 1004-1023.
Rember, R. D., and J. H. Trefry (2004), Increased concentrations of dissolved trace metals and organic carbon during snowmelt in rivers of the alaskan arctic 1 1Associate editor: K. F. Falkner, *Geochim. Cosmochim. Acta*, *68*(3), 477-489.
Romanovsky, V. E., et al. (2010), Thermal state of permafrost in Russia, *Permafrost and Periglacial Processes*, *21*(2), 136-155.
Scholz, F., and H. Kahlert (2015), The calculation of the solubility of metal hydroxides, oxide-hydroxides, and oxides, and their visualisation in logarithmic diagrams, *ChemTexts*, *1*(1), 7.
Schuur, E. A. G., et al. (2015), Climate change and the permafrost carbon feedback, *Nature*, *520*, 171.
Sidorchuk, A., and V. Grigorev (1998), *Soil erosion on the Yamal peninsula (Russian Arctic) due to gas field exploitation*, 805-811 pp.
Smith, S. L., V. E. Romanovsky, A. G. Lewkowicz, C. R. Burn, M. Allard, G. D. Clow, K. Yoshikawa, and J. Throop (2010), Thermal state of permafrost in North America: a contribution to the international polar year, *Permafrost and Periglacial Processes*, *21*(2), 117-135.
Street, L. E., J. F. Dean, M. F. Billett, R. Baxter, K. J. Dinsmore, J. S. Lessels, J.-A. Subke, D.

Tetzlaff, and P. A. Wookey (2016), Redox dynamics in the active layer of an Arctic headwater catchment; examining the potential for transfer of dissolved methane from soils to stream water, *Journal of Geophysical Research: Biogeosciences*, *121*(11), 2776-2792.

Tarnocai, C. (2009), Arctic Permafrost Soils, in *Permafrost Soils*, edited by R. Margesin, pp. 3-16, Springer Berlin Heidelberg, Berlin, Heidelberg.

Vasil'chuk, Y., N. Budantseva, A. Vasil'chuk, J. Chizhova, Y. Podborny, and J. Vasil'chuk (2016), Holocene multistage massive ice, Sabettayakha river mouth, Yamal Peninsula, northwest Siberia, *GeoResJ*, *9-12*, 54-66.

Vasyukova, E. V., O. S. Pokrovsky, J. Viers, P. Oliva, B. Dupré, F. Martin, and F. Candaudap (2010), Trace elements in organic- and iron-rich surficial fluids of the boreal zone: Assessing colloidal forms via dialysis and ultrafiltration, *Geochim. Cosmochim. Acta*, *74*(2), 449-468.

Walvoord, M. A., and R. G. Striegl (2007), Increased groundwater to stream discharge from permafrost thawing in the Yukon River basin: Potential impacts on lateral export of carbon and nitrogen, *Geophysical Research Letters*, *34*(12).

Wild, B., A. Andersson, L. Broder, J. Vonk, G. Hugelius, J. W. McClelland, W. Song, P. A. Raymond, and O. Gustafsson (2019), Rivers across the Siberian Arctic unearth the patterns of carbon release from thawing permafrost, *Proceedings of the National Academy of Sciences of the United States of America*, *116*(21), 10280-10285.

WRB (2015), World reference base (WRB) for soil resources, International soil classification system for naming soils and creating legends for soil maps., *Food and Agriculture organization of the united nation (FAO), Rome*.

Yang, D. Q., D. L. Kane, L. D. Hinzman, X. B. Zhang, T. J. Zhang, and H. C. Ye (2002), Siberian Lena River hydrologic regime and recent change, *Journal of Geophysical Research-Atmospheres*, *107*(D23).

Zheng, L., I. Overeem, K. Wang, and G. D. Clow (2019), Changing Arctic River Dynamics Cause Localized Permafrost Thaw, *Journal of Geophysical Research-Earth Surface*, *124*(9), 2324-2344.

Figure captions

Figure 1. Location of the sampling area and installed thermometer (**A**). Soil pit profiles and their upper vegetation species near rivers: (**B**) Taz river (67°30'13.3"N, 78°40'56.2"E), (**C**) Syoyakha river (69°57'03.6"N, 71°23'15.2"E), and (**D**) Murtyyakha river (70°06'04.7"N, 68°40'24.1"E) in Yamal-Nets Autonomous Region. All soil profiles are gleyed and have oxidation/reduction horizons in the upper active layer, substantial top organic layer, and cryoturbation in the lower part of the active layer.

Figure 2. Vertical metal/element distribution in soil cores collected from TA (Taz river), SY (Syoyakha river) and MU (Murtyyakha river) sites in the Yamal-Nets Autonomous Region in beginning May 2016. The logarithmic transformed distribution shows the elements' enrichment relevant to the top layer with humus accumulation in an oxidizing condition (Mn and Co) and the lower gleyed layer in a reducing condition.

Figure 3. Distributions of soluble metals along the vertical soil water extracted from the soil cores collected adjacent to the Ta, Sy, and Mu rivers in the Yamal-Nets Autonomous Region.

Figure 4. Soil temperature (℃) at different soil depths within the active layer as function of time in 2016. The soil in the Russian Arctic (TA, SY, and MU sites) experiences a top to down freezing process, making soil porewater flow downwards to deeper soils above frozen materials (permafrost table).

Figure 5. Soluble element concentrations (μg/L) in the supra-permafrost water collected from the Ta, Sy and Mu sites as a function of date in 2016, respectively.

Figure 6. Soluble element concentrations (μg/L) in the surface water from connected hydrological streams to rivers and rivers from the TA, SY, and MU sites as a function of date in 2016, respectively.

Figure 7. Plot of partition coefficients (K_d) for the soil cores from the TA, SY, and MU sites, sampled in the late September 2016. K_d values were calculated by the ratio of elemental concentrations (mg/kg) in the solid soil phase to the elemental concentrations (mg/L) in soil porewater.

Figure 8. Elements/CO_2/CH_4-dissolved organic carbon (DOC) relationships for the surrounding hydrological streams in TA, SY, and MU sites over the course of spring to autumn 2016.

Figure 9. Linear correlations of the elements with high mobility in soil columns between the connected surface streams and receiving rivers.

Figure 10. Linear correlations of the elements with high mobility in soil column between the connected surface streams and supra-permafrost water.

Figure 1.

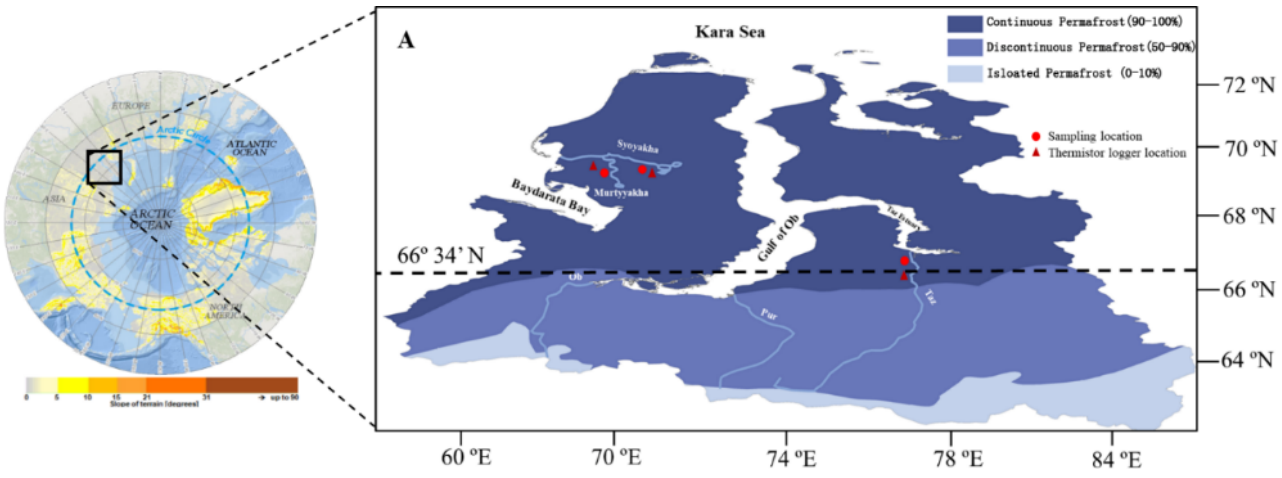
A
Kara Sea
Continuous Permafrost (90–100%)
Discontinuous Permafrost (50–90%)
Isloated Permafrost (0–10%)
Sampling location
Thermistor logger location
Syoyakha
Murtyyakha
Baydarata Bay
Gulf of Ob
Ob
Taz
Pur
66° 34' N
72 °N
70 °N
68 °N
66 °N
64 °N
60 °E
70 °E
74 °E
78 °E
84 °E
EUROPE
ATLANTIC OCEAN
ASIA
ARCTIC OCEAN
Arctic Circle
Slope of terrain [degrees]

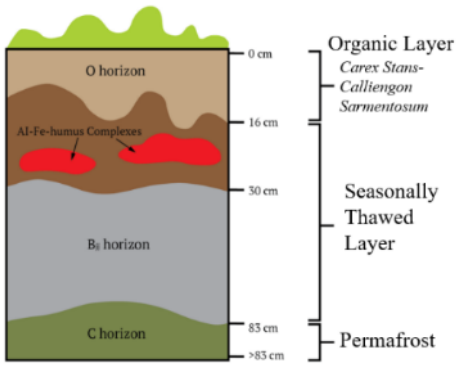
B
O horizon
Al-Fe-humus Complexes
Bf horizon
C horizon
0 cm
16 cm
30 cm
83 cm
>83 cm
Organic Layer
Carex Stans-
Calliengon
Sarmentosum
Seasonally
Thawed
Layer
Permafrost

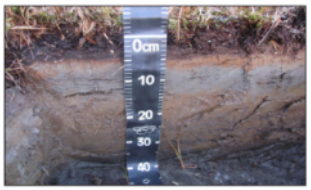

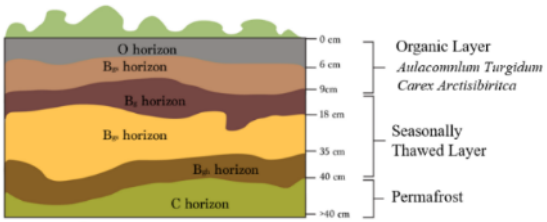
C
O horizon
Bfp horizon
Bf horizon
Bfp horizon
Bgf horizon
C horizon
0 cm
6 cm
9cm
18 cm
35 cm
40 cm
>40 cm
Organic Layer
Aulacomnium Turgidum
Carex Arctisibirica
Seasonally
Thawed Layer
Permafrost

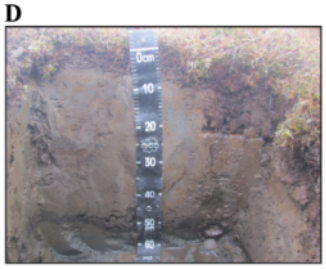

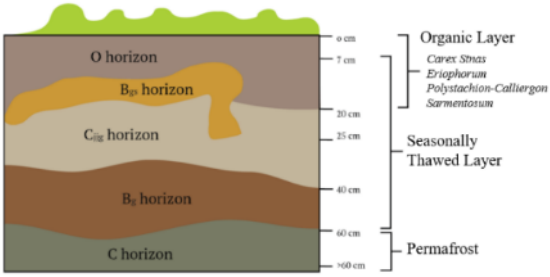
D
O horizon
Bgf horizon
Cfg horizon
Bg horizon
C horizon
0 cm
7 cm
20 cm
25 cm
40 cm
60 cm
>60 cm
Organic Layer
Carex Stnax
Eriophorum
Polystachion-Calliergon
Sarmentosum
Seasonally
Thawed Layer
Permafrost

Figure 2.

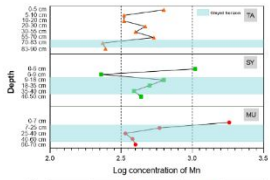
Depth
TA
SY
MU
Gleyed horizon
Log concentration of Mn

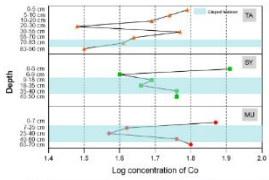
Depth
TA
SY
MU
Gleyed horizon
Log concentration of Co

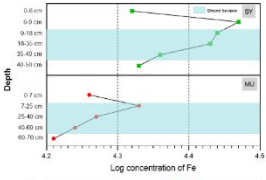
Depth
SY
MU
Gleyed horizon
Log concentration of Fe

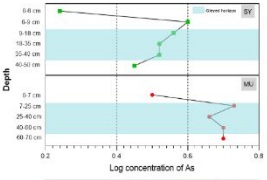
Depth
SY
MU
Gleyed horizon
Log concentration of As

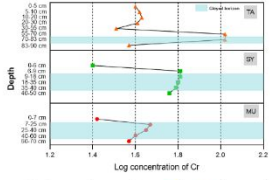
Depth
TA
SY
MU
Gleyed horizon
Log concentration of Cr

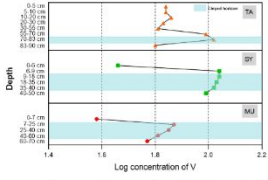
Depth
TA
SY
MU
Gleyed horizon
Log concentration of V

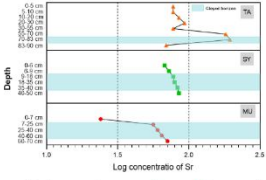
Depth
TA
SY
MU
Gleyed horizon
Log concentratio of Sr

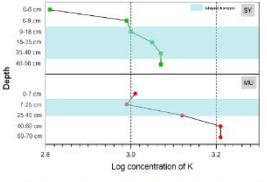
Depth
SY
MU
Gleyed horizon
Log concentration of K

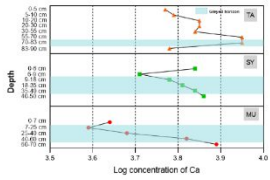
Depth
TA
SY
MU
Gleyed horizon
Log concentration of Ca

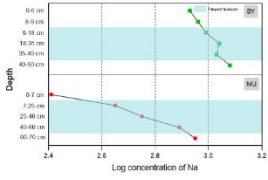
Depth
SY
MU
Gleyed horizon
Log concentration of Na

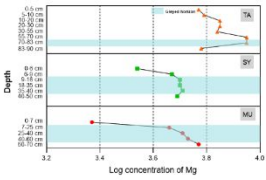
Depth
TA
SY
MU
Gleyed horizon
Log concentration of Mg

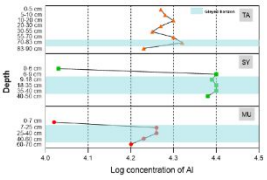
Depth
TA
SY
MU
Gleyed horizon
Log concentration of Al

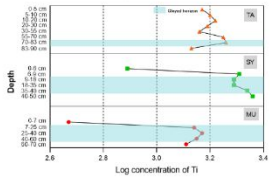
Depth
TA
SY
MU
Gleyed horizon
Log concentration of Ti

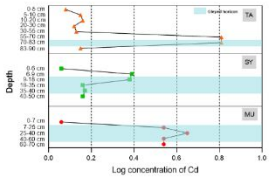
Depth
TA
SY
MU
Gleyed horizon
Log concentration of Cd

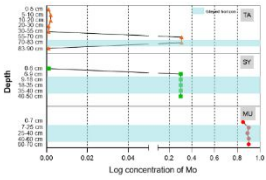
Depth
TA
SY
MU
Gleyed horizon
Log concentration of Mo

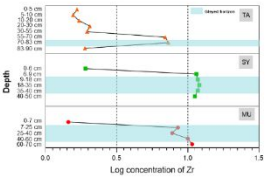
Depth
TA
SY
MU
Gleyed horizon
Log concentration of Zr

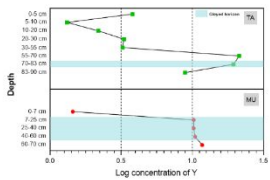
Depth
TA
SY
MU
Gleyed horizon
Log concentration of Y

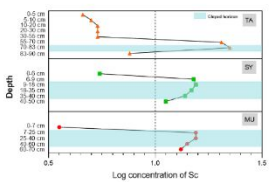
Depth
TA
SY
MU
Gleyed horizon
Log concentration of Sc

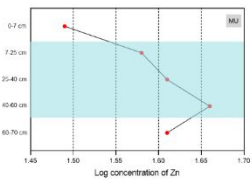
Depth
MU
Log concentration of Zn

Figure 3.

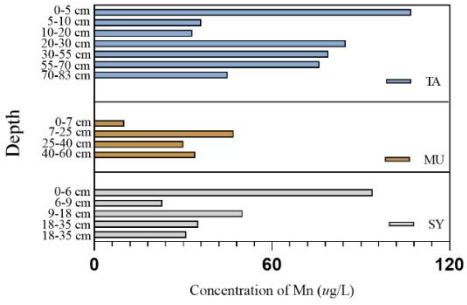
Depth
0-5 cm
5-10 cm
10-20 cm
20-30 cm
30-55 cm
55-70 cm
70-83 cm
TA
0-7 cm
7-25 cm
25-40 cm
40-60 cm
MU
0-6 cm
6-9 cm
9-18 cm
18-35 cm
18-35 cm
SY
0
60
120
Concentration of Mn (ug/L)

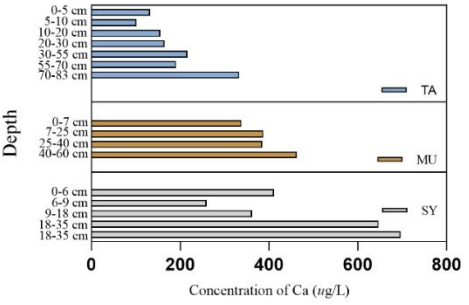
Depth
0-5 cm
5-10 cm
10-20 cm
20-30 cm
30-55 cm
55-70 cm
70-83 cm
TA
0-7 cm
7-25 cm
25-40 cm
40-60 cm
MU
0-6 cm
6-9 cm
9-18 cm
18-35 cm
18-35 cm
SY
0
200
400
600
800
Concentration of Ca (ug/L)

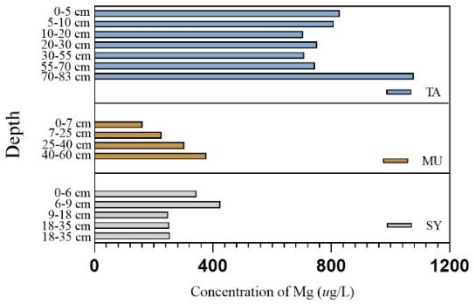
Depth
0-5 cm
5-10 cm
10-20 cm
20-30 cm
30-55 cm
55-70 cm
70-83 cm
TA
0-7 cm
7-25 cm
25-40 cm
40-60 cm
MU
0-6 cm
6-9 cm
9-18 cm
18-35 cm
18-35 cm
SY
0
400
800
1200
Concentration of Mg (ug/L)

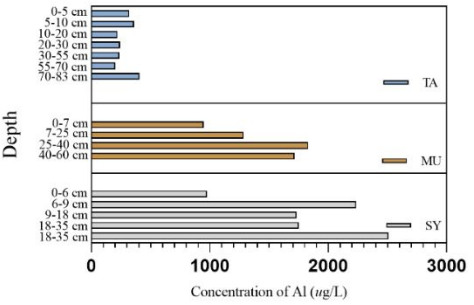
Depth
0-5 cm
5-10 cm
10-20 cm
20-30 cm
30-55 cm
55-70 cm
70-83 cm
TA
0-7 cm
7-25 cm
25-40 cm
40-60 cm
MU
0-6 cm
6-9 cm
9-18 cm
18-35 cm
18-35 cm
SY
0
1000
2000
3000
Concentration of Al (ug/L)

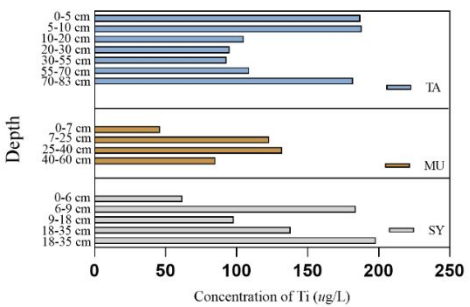
Depth
0-5 cm
5-10 cm
10-20 cm
20-30 cm
30-55 cm
55-70 cm
70-83 cm
TA
0-7 cm
7-25 cm
25-40 cm
40-60 cm
MU
0-6 cm
6-9 cm
9-18 cm
18-35 cm
18-35 cm
SY
0
50
100
150
200
250
Concentration of Ti (ug/L)

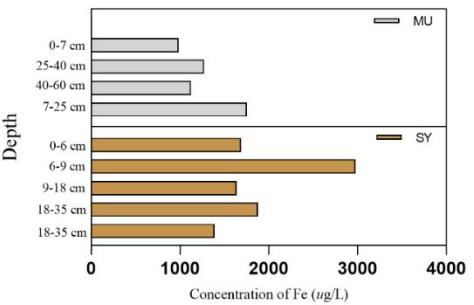
Depth
MU
0-7 cm
25-40 cm
40-60 cm
7-25 cm
SY
0-6 cm
6-9 cm
9-18 cm
18-35 cm
18-35 cm
0
1000
2000
3000
4000
Concentration of Fe (ug/L)

Figure 4.

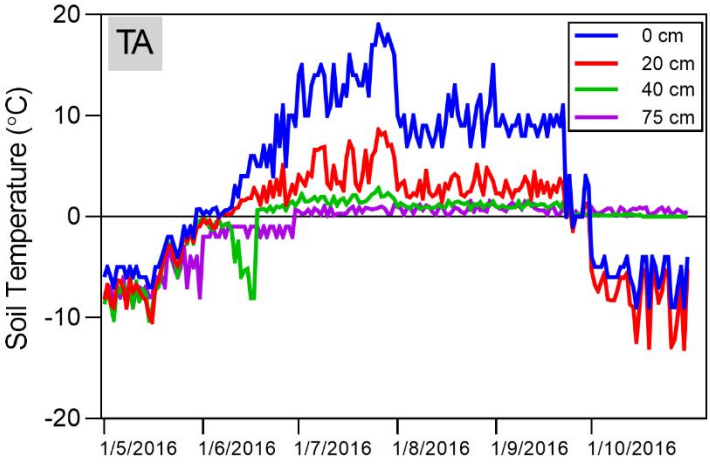
TA
0 cm
20 cm
40 cm
75 cm
Soil Temperature (°C)
20
10
0
-10
-20
1/5/2016
1/6/2016
1/7/2016
1/8/2016
1/9/2016
1/10/2016

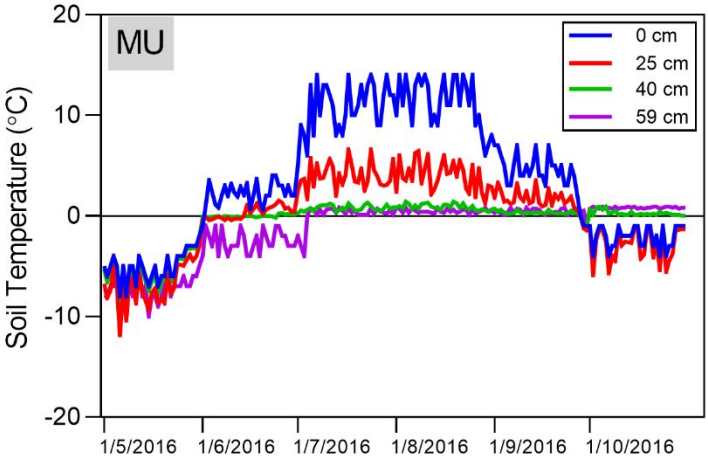
MU
0 cm
25 cm
40 cm
59 cm
Soil Temperature (°C)
20
10
0
-10
-20
1/5/2016
1/6/2016
1/7/2016
1/8/2016
1/9/2016
1/10/2016

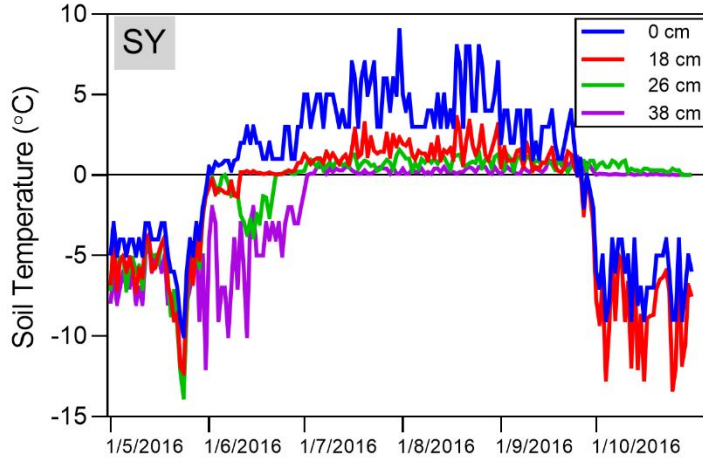
SY
0 cm
18 cm
26 cm
38 cm
Soil Temperature (°C)
10
5
0
-5
-10
-15
1/5/2016
1/6/2016
1/7/2016
1/8/2016
1/9/2016
1/10/2016

Figure 5.

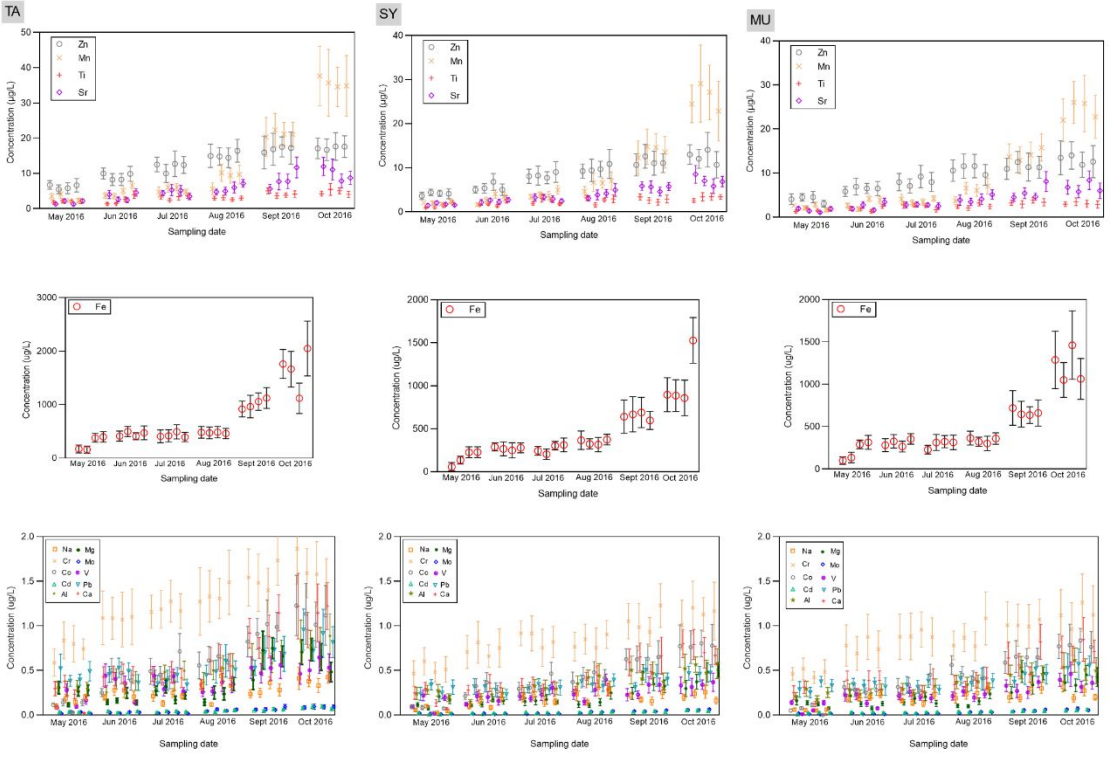
TA
SY
MU
Zn
Mn
Ti
Sr
Fe
Na
Mg
Cr
Mo
Co
V
Cd
Pb
Al
Ca
Concentration (μg/L)
Sampling date
May 2016
Jun 2016
Jul 2016
Aug 2016
Sept 2016
Oct 2016

Figure 6.

TA

Surface flow

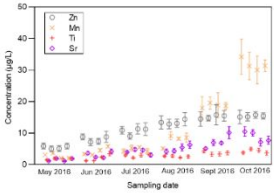

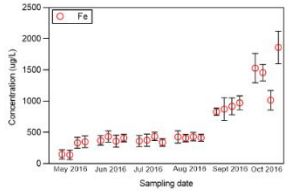

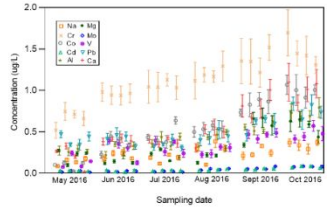

River

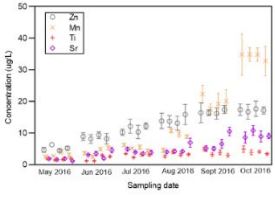

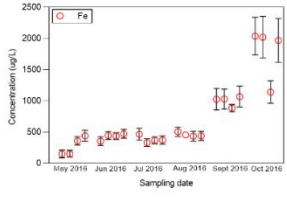

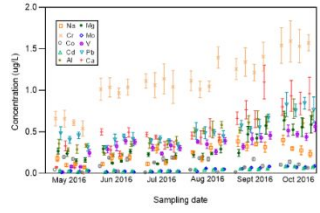

MU

Surface flow

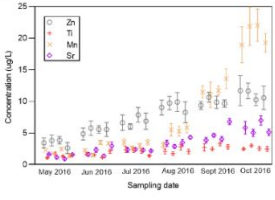

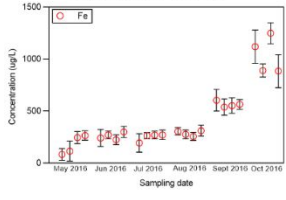

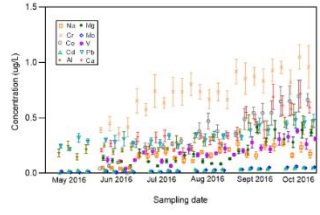

River

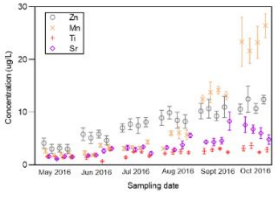

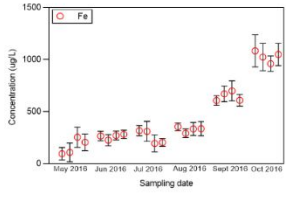

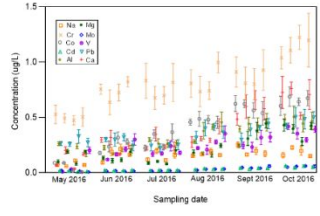

SY

Surface flow

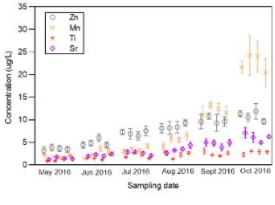

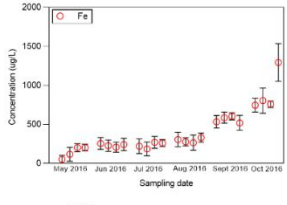

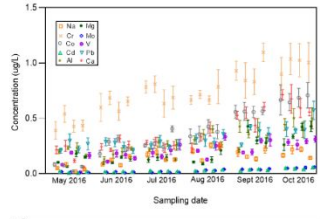

River

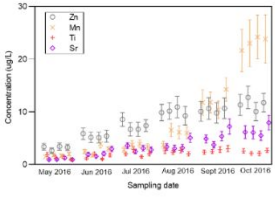

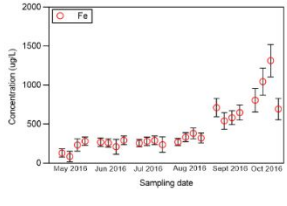

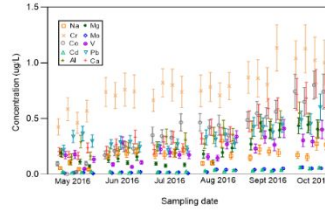

Figure 7.

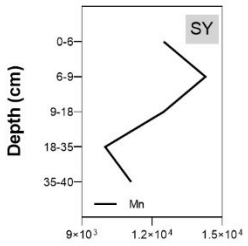
SY
Depth (cm)
0-6
6-9
9-18
18-35
35-40
Mn
9×10³ 1.2×10⁴ 1.5×10⁴

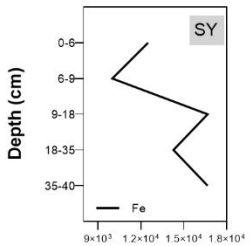
SY
Depth (cm)
0-6
6-9
9-18
18-35
35-40
Fe
9×10³ 1.2×10⁴ 1.5×10⁴ 1.8×10⁴

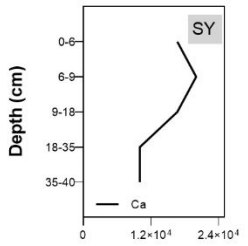
SY
Depth (cm)
0-6
6-9
9-18
18-35
35-40
Ca
0 1.2×10⁴ 2.4×10⁴

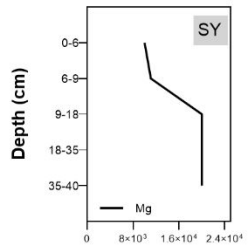
SY
Depth (cm)
0-6
6-9
9-18
18-35
35-40
Mg
0 8×10³ 1.6×10⁴ 2.4×10⁴

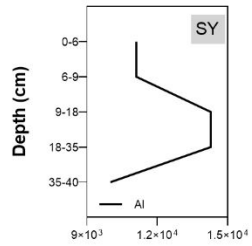
SY
Depth (cm)
0-6
6-9
9-18
18-35
35-40
Al
9×10³ 1.2×10⁴ 1.5×10⁴

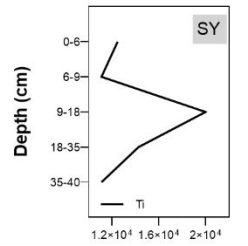
SY
Depth (cm)
0-6
6-9
9-18
18-35
35-40
Ti
1.2×10⁴ 1.6×10⁴ 2×10⁴

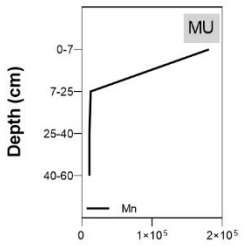
MU
Depth (cm)
0-7
7-25
25-40
40-60
Mn
0 1×10⁵ 2×10⁵

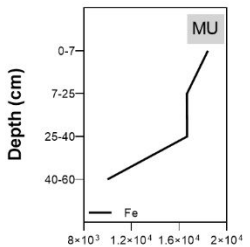
MU
Depth (cm)
0-7
7-25
25-40
40-60
Fe
8×10³ 1.2×10⁴ 1.6×10⁴ 2×10⁴

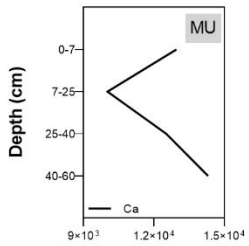
MU
Depth (cm)
0-7
7-25
25-40
40-60
Ca
9×10³ 1.2×10⁴ 1.5×10⁴

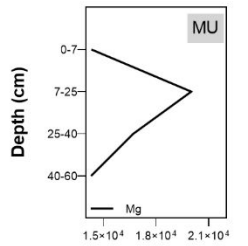
MU
Depth (cm)
0-7
7-25
25-40
40-60
Mg
1.5×10⁴ 1.8×10⁴ 2.1×10⁴

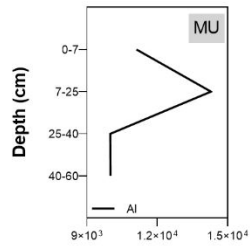
MU
Depth (cm)
0-7
7-25
25-40
40-60
Al
9×10³ 1.2×10⁴ 1.5×10⁴

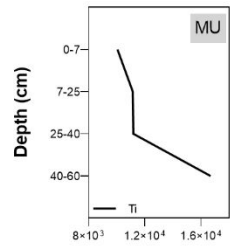
MU
Depth (cm)
0-7
7-25
25-40
40-60
Ti
8×10³ 1.2×10⁴ 1.6×10⁴

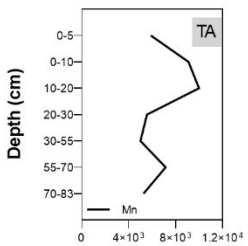
TA
Depth (cm)
0-5
0-10
10-20
20-30
30-55
55-70
70-83
Mn
0 4×10³ 8×10³ 1.2×10⁴

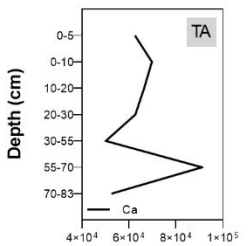
TA
Depth (cm)
0-5
0-10
10-20
20-30
30-55
55-70
70-83
Ca
4×10⁴ 6×10⁴ 8×10⁴ 1×10⁵

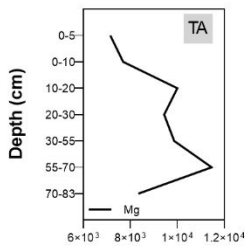
TA
Depth (cm)
0-5
0-10
10-20
20-30
30-55
55-70
70-83
Mg
6×10³ 8×10³ 1×10⁴ 1.2×10⁴

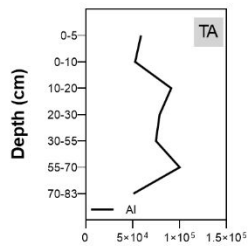
TA
Depth (cm)
0-5
0-10
10-20
20-30
30-55
55-70
70-83
Al
0 5×10⁴ 1×10⁵ 1.5×10⁵

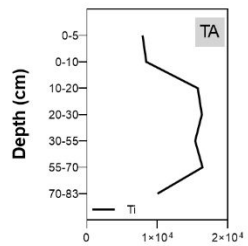
TA
Depth (cm)
0-5
0-10
10-20
20-30
30-55
55-70
70-83
Ti
0 1×10⁴ 2×10⁴

Figure 8.

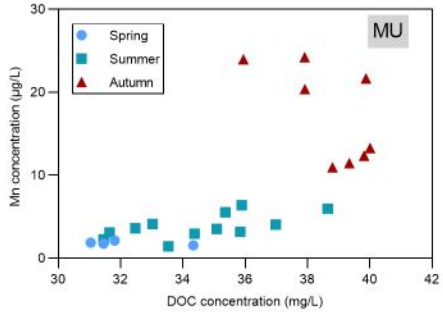
MU
Spring
Summer
Autumn
Mn concentration (μg/L)
DOC concentration (mg/L)

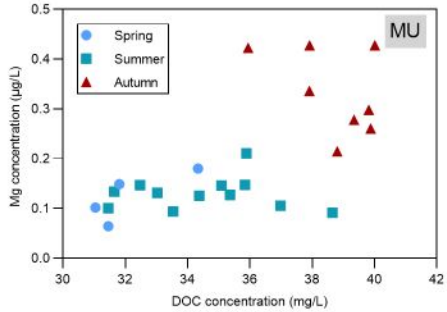
MU
Spring
Summer
Autumn
Mg concentration (μg/L)
DOC concentration (mg/L)

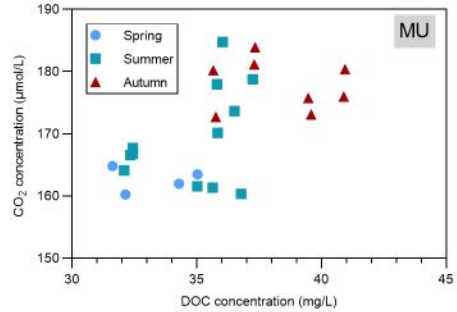
MU
Spring
Summer
Autumn
CO2 concentration (μmol/L)
DOC concentration (mg/L)

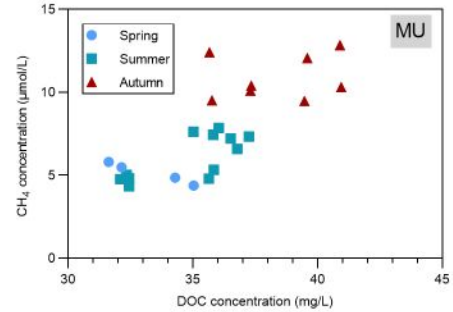
MU
Spring
Summer
Autumn
CH4 concentration (μmol/L)
DOC concentration (mg/L)

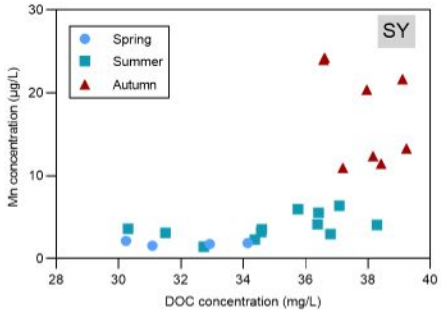
SY
Spring
Summer
Autumn
Mn concentration (μg/L)
DOC concentration (mg/L)

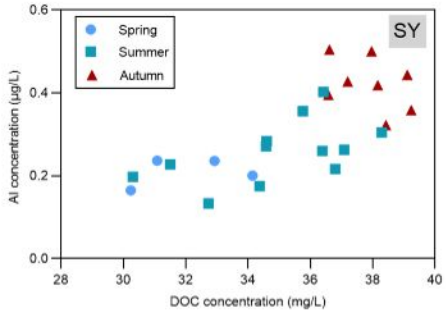
SY
Spring
Summer
Autumn
Al concentration (μg/L)
DOC concentration (mg/L)

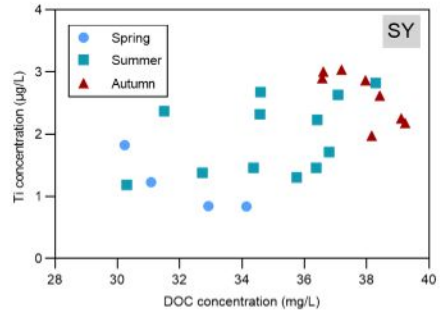
SY
Spring
Summer
Autumn
Ti concentration (μg/L)
DOC concentration (mg/L)

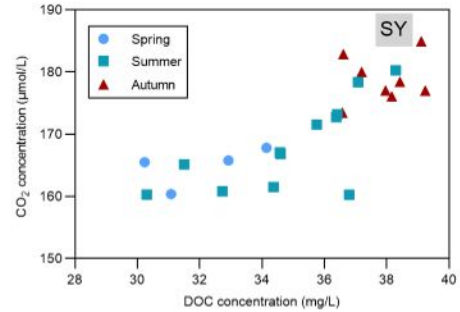
SY
Spring
Summer
Autumn
CO2 concentration (μmol/L)
DOC concentration (mg/L)

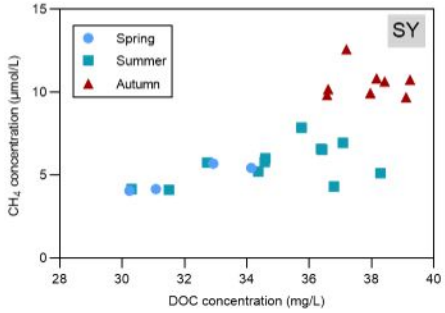
SY
Spring
Summer
Autumn
CH4 concentration (μmol/L)
DOC concentration (mg/L)

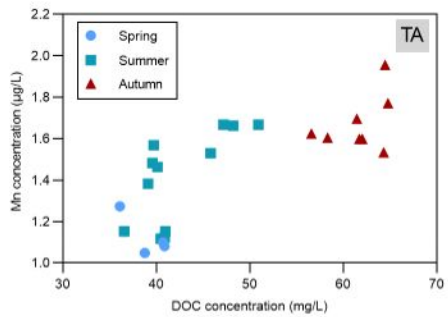
TA
Spring
Summer
Autumn
Mn concentration (μg/L)
DOC concentration (mg/L)

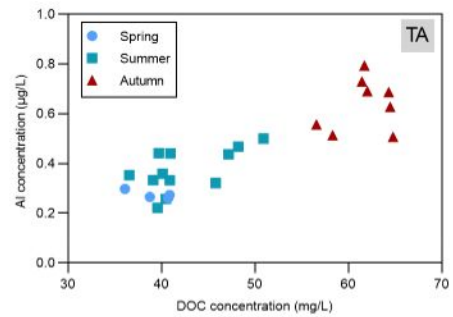
TA
Spring
Summer
Autumn
Al concentration (μg/L)
DOC concentration (mg/L)

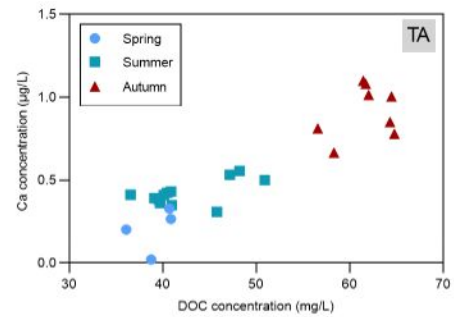
TA
Spring
Summer
Autumn
Ca concentration (μg/L)
DOC concentration (mg/L)

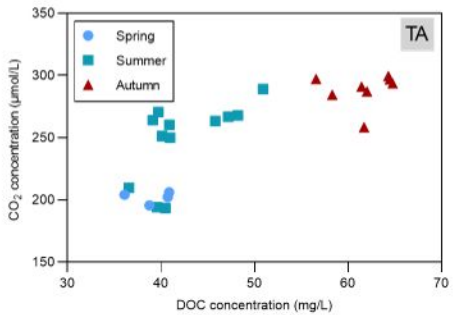
TA
Spring
Summer
Autumn
CO2 concentration (μmol/L)
DOC concentration (mg/L)

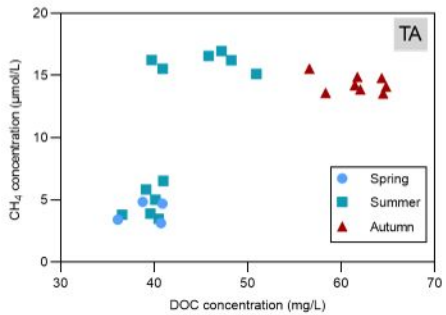
TA
Spring
Summer
Autumn
CH4 concentration (μmol/L)
DOC concentration (mg/L)

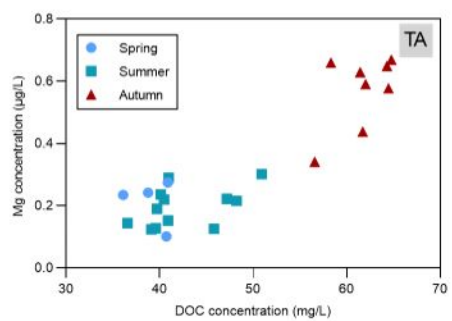
TA
Spring
Summer
Autumn
Mg concentration (μg/L)
DOC concentration (mg/L)

Figure 9.

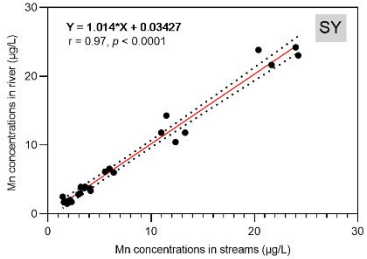
Y = 1.014*X + 0.03427
r = 0.97, p < 0.0001
SY
Mn concentrations in river (μg/L)
Mn concentrations in streams (μg/L)

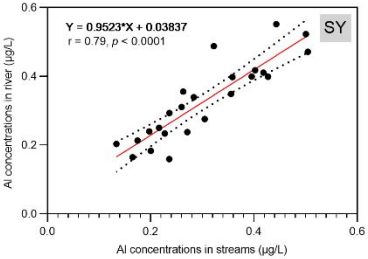
Y = 0.9523*X + 0.03837
r = 0.79, p < 0.0001
SY
Al concentrations in river (μg/L)
Al concentrations in streams (μg/L)

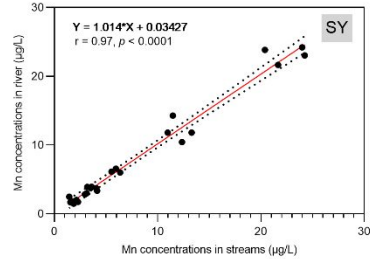
Y = 1.014*X + 0.03427
r = 0.97, p < 0.0001
SY
Mn concentrations in river (μg/L)
Mn concentrations in streams (μg/L)

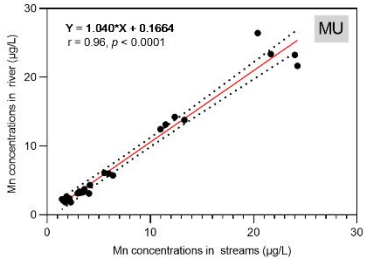
Y = 1.040*X + 0.1664
r = 0.96, p < 0.0001
MU
Mn concentrations in river (μg/L)
Mn concentrations in streams (μg/L)

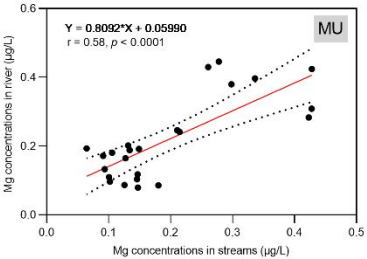
Y = 0.8092*X + 0.05990
r = 0.58, p < 0.0001
MU
Mg concentrations in river (μg/L)
Mg concentrations in streams (μg/L)

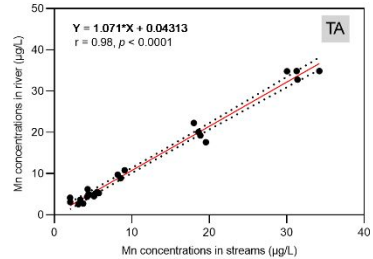
Y = 1.071*X + 0.04313
r = 0.98, p < 0.0001
TA
Mn concentrations in river (μg/L)
Mn concentrations in streams (μg/L)

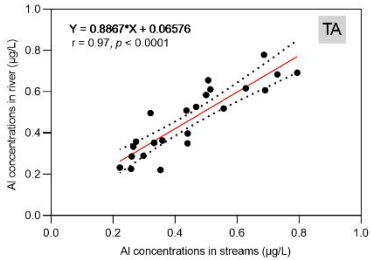
Y = 0.8867*X + 0.06576
r = 0.97, p < 0.0001
TA
Al concentrations in river (μg/L)
Al concentrations in streams (μg/L)

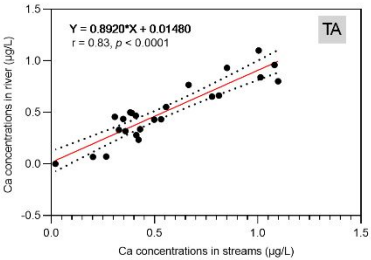
Y = 0.8920*X + 0.01480
r = 0.83, p < 0.0001
TA
Ca concentrations in river (μg/L)
Ca concentrations in streams (μg/L)

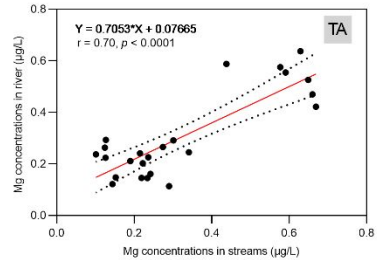
Y = 0.7053*X + 0.07665
r = 0.70, p < 0.0001
TA
Mg concentrations in river (μg/L)
Mg concentrations in streams (μg/L)

Figure 10.

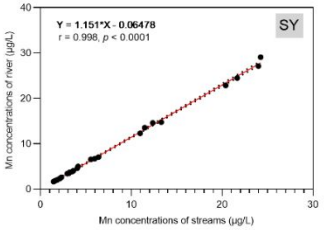
Y = 1.151*X - 0.06478
r = 0.998, p < 0.0001
SY
Mn concentrations of river (μg/L)
Mn concentrations of streams (μg/L)

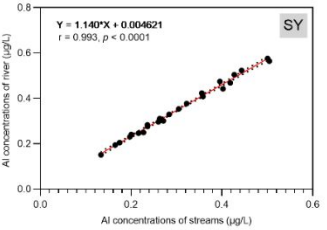
Y = 1.140*X + 0.004621
r = 0.993, p < 0.0001
SY
Al concentrations of river (μg/L)
Al concentrations of streams (μg/L)

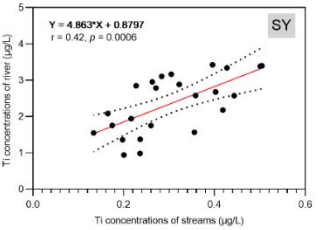
Y = 4.863*X + 0.8797
r = 0.42, p = 0.0006
SY
Ti concentrations of river (μg/L)
Ti concentrations of streams (μg/L)

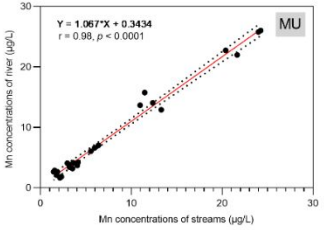
Y = 1.067*X + 0.3434
r = 0.98, p < 0.0001
MU
Mn concentrations of river (μg/L)
Mn concentrations of streams (μg/L)

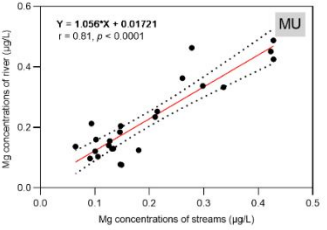
Y = 1.056*X + 0.01721
r = 0.81, p < 0.0001
MU
Mg concentrations of river (μg/L)
Mg concentrations of streams (μg/L)

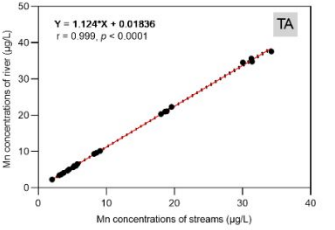
Y = 1.124*X + 0.01836
r = 0.999, p < 0.0001
TA
Mn concentrations of river (μg/L)
Mn concentrations of streams (μg/L)

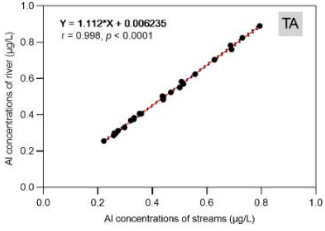
Y = 1.112*X + 0.006235
r = 0.998, p < 0.0001
TA
Al concentrations of river (μg/L)
Al concentrations of streams (μg/L)

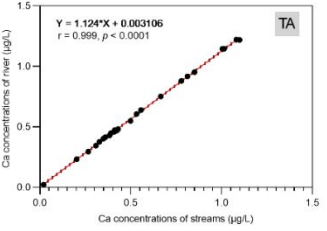
Y = 1.124*X + 0.003106
r = 0.999, p < 0.0001
TA
Ca concentrations of river (μg/L)
Ca concentrations of streams (μg/L)

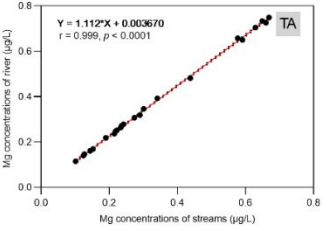
Y = 1.112*X + 0.003670
r = 0.999, p < 0.0001
TA
Mg concentrations of river (μg/L)
Mg concentrations of streams (μg/L)